Desalination 620 (2026) 119643

Contents lists available at ScienceDirect

Desalination

journal homepage: www.elsevier.com/locate/desal

Functionalized MXene-reinforced PPO-based nanocomposite anion exchange membranes for high-performance water electrolysis

Mohammad Mahbub Kabir [a,b], M.A. Zaed [c], Yeshi Choden [a,b], R. Saidur [c,e], Leonard Tijing [a,b], Sherub Phuntsho [a,b], Sang Yong Nam [d], Ho Kyong Shon [a,*]

[a] ARC Research Hub for Nutrients in a Circular Economy, School of Civil and Environmental Engineering, University of Technology Sydney, P.O. Box 123, 15 Broadway, NSW, 2007, Australia
[b] Centre for Technology in Water and Wastewater, School of Civil and Environmental Engineering, University of Technology Sydney, P.O. Box 123, 15 Broadway, NSW, 2007, Australia
[c] Research Centre for Nanomaterials and Energy Technology (RCNMET), Faculty of Engineering and Technology, Sunway University, No. 5, Jalan Universiti, Bandar Sunway, 47500, Selangor, Darul Ehsan, Malaysia
[d] Department of Materials Engineering and Convergence Technology, Gyeongsang National University, Jinju, 52828, Republic of Korea
[e] School of Engineering, Lancaster University, Lancaster LA1 4YW, UK

HIGHLIGHTS

- Nanocomposite AEM for high-performance water electrolysis.
- Addressed key trade-offs between electrochemical, dimensional and mechanical attributes of AEMs.
- QPPO-NH_4-Mx-3.0 demonstrated an impressive ion conductivity of 153.2 mS cm^{-1}.
- Recorded peak current density of 2.1 A cm^{-2} at 2 V in 1 M KOH at 60 °C.
- Durability testing validated robust cell performance with a minimal voltage decay rate.

GRAPHICAL ABSTRACT

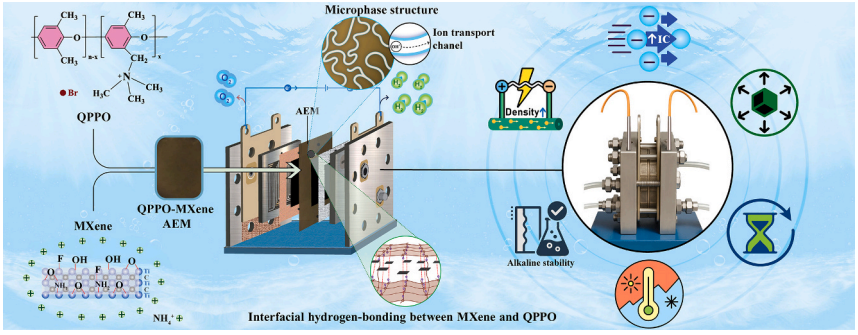

ARTICLE INFO

Keywords:
MXene
Nanocomposite membranes
Microphase separation
OH^- exchange
Poly(phenyl oxide)
Hydrogen production

ABSTRACT

One of the major challenges in advancing anion exchange membrane water electrolysis (AEMWE) lies in addressing the trade-offs between dimensional stability, electrochemical performance, and mechanical integrity of anion exchange membranes (AEMs). Overcoming these trade-offs is crucial for improving the performance and reliability of AEMWE systems. In this study, we addressed this challenge by developing a series of nanocomposite AEMs by reinforcing quaternized poly(phenylene oxide) (QPPO) with ammonium-functionalized MXene (NH_4^+-$Ti_3C_2T_x$). The resulting membranes exhibited significant enhancement in dimensional stability, electrochemical performance, mechanical strength, and thermal stability compared to the pristine QPPO membrane. Among the composite AEMs, QPPO-NH_4-Mx-3.0 demonstrated the notable overall performance, achieving an impressive hydroxide (OH^-) ion conductivity (IC) of 153.2 mS cm^{-1} at 80 °C-2.5 times higher than that of virgin QPPO. Additionally, the membrane contributed excellent tensile strength of 61.2 MPa, 4 times greater than that of the pristine QPPO, and achieved a peak current density of 2.1 A cm^{-2} at 2 V in 1 M KOH at 60 °C. The membrane

* Corresponding author.
E-mail address: Hokyong.Shon-1@uts.edu.au (H.K. Shon).

https://doi.org/10.1016/j.desal.2025.119643
Received 30 August 2025; Received in revised form 30 October 2025; Accepted 15 November 2025
Available online 21 November 2025

also showcased exceptional alkaline stability, retaining 80.2 % of its initial IC after three weeks of immersion in 1 M KOH. Durability testing further validated its robustness, achieved a stable operation maintained up to 150 h of electrolysis with a minimal voltage decay rate of 1.5 mV h^{-1}. In summary, the QPPO-NH_4-Mx-3.0 demonstrates substantial promise as a high-performance AEM for advancing AEMWE technology, paving the way for more efficient and reliable water electrolysis systems.

1. Introduction

Energy is the cornerstone of human progress, powering advancements in every aspect of society. The rapid increase in global energy demand is driven by industrial growth, urbanization, and improved living standards, all of which are closely tied to population growth [1,2]. Currently, fossil fuels (FFs) dominate the global energy mix, accounting for 81–82 % of total energy consumption. However, their extensive use is a leading contributor to greenhouse gas (GHG) emissions, exacerbating the ongoing climate crisis [3–5]. This dependency underscores the urgent need to transition toward cleaner, more sustainable energy solutions that align with the United Nations' sustainable development goals (SDGs). Hydrogen has emerged as a promising green energy carrier, offering significant potential to revolutionize the energy systems due to its high energy density, environmental benefits, and a broad range of applications [6–8]. With an energy density surpassing that of gasoline at standard conditions and the ability to be stored for future use, hydrogen has garnered increasing global attention [9]. Its integration into energy systems is recognized as vital to achieving net-zero emissions by 2050. Substantial research efforts are, therefore, being directed toward developing technologies to harness hydrogen's potential as a sustainable energy source [10,11]. Among these technologies, water electrolysis (WE) has gained prominence as an efficient and environmentally friendly technique for producing green hydrogen [3,11].

WE splits water into hydrogen (H_2) and oxygen (O_2) through an electrochemical process, offering benefits such as high efficiency, ultrapure hydrogen and oxygen production, and a relatively simple operational se-tup [3,4]. Existing WE systems can be broadly categorized into three types: alkaline water electrolysis (AWE), proton exchange membrane water electrolysis (PEMWE), and anion exchange membrane water electrolysis (AEMWE) [3,4,8]. AWE is a mature and commercially established technology; however, it is constrained by the corrosive nature of liquid alkaline electrolytes and low current densities due to the limited mobility of hydroxide (OH^-) ions [4,6,12]. PEMWE offers higher performance but faces challenges related to its reliance on expensive noble metal catalysts and the fast degradation of these materials over time [3,13]. In contrast, AEMWE has emerged as a cost-effective alternative, operating efficiently with non-noble metal catalysts in alkaline conditions, which enhance ion transport kinetics and reduce operational costs [12,14]. However, AEMWE technologies still suffer from performance degradation, long-term stability, and limited ion conductivity (IC), which must be addressed to realize their full potential [4,6,12,15].

A critical component in the success of AEMWE systems is the anion exchange membrane (AEM), which determines the overall efficiency, stability, and durability of the AEM-based electrolyzer. An ideal AEM should possess high IC, robust mechanical strength, thermal and chemical stability, and resistance to alkaline degradation. However, achieving a balance among these properties is a persistent challenge, as trade-offs often arise during membrane development [15,1616,101–103]. Polymer-based membranes, such as those derived from poly (phenylene oxide) (PPO), offer a promising pathway for AEM development due to their availability, cost-effectiveness, and inherent thermal and mechanical stability [17]. Despite these advantages, PPO-based membranes often suffer from low IC and structural degradation under alkaline conditions, limiting their application in AEMWE [18].

Diverse nanomaterials were explored in the literature to synthesize the PPO-based composite AEMs for WE and fuel cell (FC), i.e., silicon dioxide (SiO_2), graphene oxide (GO), cellulose, layered double hydroxide (LDH), metal-organic framework (MOF), covalent organic framework (COF), zeolitic imidazole framework-8 (ZIF-8), to name but a few. Applications of these materials in AEMs development have both promise and limitations [19–25,100]. For example, Xu et al. [26] developed a PPO-based AEM using a long-chain bis-imidazolium cross-linker. This membrane exhibited a low IC of 24.10 mS cm^{-1} but demonstrated enhanced alkaline stability, retaining 78 % of its initial IC after 480 h in 2 M NaOH. Likewise, another cross-linked macromolecular AEM achieved an IC of 80 mS cm^{-1}, with 75 % residual IC kept after 1000 h in 1 M NaOH [27]. A hybrid AEM combining COF with PPO exhibited an impressive IC of 168 mS cm^{-1}. However, this membrane suffered from poor mechanical performance, limiting its practical applications [24]. Chen et al. [25] designed a PPO-based AEM incorporating functionalized COF and GO. Although the QAmCOF-LZU1/PPO-5.0 membrane achieved excellent IC, but it exhibited very low mechanical integrity, highlighting the trade-off between electrochemical performance and mechanical stability [28]. Addressing these limitations is essential for advancing PPO-based AEMWE technologies.

In recent years, MXene, a classical two-dimensional (2D) nanomaterial composed of transition metal carbides, nitrides, or carbonitrides, have demonstrated significant potential as a nanofiller for enhancing the performances of polymer-based AEMs [14,29]. MXene possesses unique properties, including high IC, a large surface area, and tunable surface chemistry, making it ideal for improving the electrochemical performance of membranes. When incorporated into polymers, MXene facilitate advanced functionalization, boosting IC, dimensional stability, and alkaline resistance [15]. A key advantage of MXene lies in its ability to induce microphase separation (MIPS) structures within the membrane matrix. This phenomenon creates distinct hydrophilic and hydrophobic domains, enabling continuous ionic pathways for efficient ion transport while ensuring structural integrity through robust hydrophobic regions [14,15,30]. Such improvements are particularly beneficial for guaranteeing the thermal, mechanical, and chemical stability of membranes under the desired conditions of WE [30]. However, the application of MXene in PPO-based AEMs has not been reported yet for WE applications. Although MXene's potential for high-performance AEMs development for WE and FC is well documented in other polymeric materials, especially poly(aryl piperidinium). Zhang et al. developed quaternized poly(*p*-terphenylene piperidinium) (QPAP) and MXene-based AEM for FC, where QPAP/NH_4-$Mo_2Ti_2C_3Tx$ membrane demonstrated an IC of 121 mS cm^{-1} with a power density of 540 mW cm^{-2}. The membrane also demonstrated excellent mechanical integrity, with a tensile strength of 68 megapascal (Mpa) [15]. Yang et al. fabricated quaternized polysulfone/polyquaternium-10 (QPSU/PQ-10) mixed matrix AEMs for FC applications, integrating LiF-Ti_3C_2Tx and NH_4HF_2-Ti_3C_2Tx MXene through semi-interpenetrating polymer network techniques. The AEMs resulted in an IC of 88.76 mS cm^{-1} with a power density of 106.28 mW cm^{-2} [31]. HF-$Ti_3C_2T_x$ MXene doped quaternized poly(aryl piperidinium) (QPAP)-based AEM exhibited an excellent IC of 159.4 mS cm^{-1} with good alkaline stability at 80 °C in 1 M NaOH [14]. However, these studies demonstrated limited cell performance and long-term durability of the AEMs.

Although MXene is currently a relatively expensive material compared to other nanomaterials, however, given the potential market size of the global hydrogen economy, large-scale production could significantly lower the cost of this material. Thus, using Mxene in composite AEMs fabrication for AEMWE might not increase the cost of

hydrogen production or the scalability of the AEMWE at an industrial scale. Despite substantial advancements in AEM development, the integration of MXene into polymer matrices, especially in PPO, remains an area of active investigation, particularly for WE and FC applications. Challenges such as achieving uniform dispersion of MXene, optimizing polymer-additive interactions, and ensuring long-term stability under operational conditions highlight the need for continued research. To address the existing trade-off issues in AEM-based WE, considering the limitations of PPO-based AEMs, this study introduces a novel strategy for developing high-performance composite AEMs by reinforcing ammonium-functionalized MXene (NH_4^+-$Ti_3C_2T_x$) into the QPPO matrix (Fig. 1). These AEMs develop the MIPS structures into the AEMs due to the MXene's hydrophilic functional groups and improved interfacial compatibility with the PPO matrices. The resulting AEMs overcome the key trade-offs, exhibiting excellent IC, stable cell performance, and improved thermal and mechanical stability under alkaline environments compared to the existing PPO-based AEMs, reported MXene-modified AEMs and some of the available commercial AEMs.

2. Experimental

2.1. Materials

Poly (2,6-dimethyl-1,4-phenylene oxide) (PPO), 2,2′-azobisisobutyronitrile (12 wt% in acetone) (AIBN), N-bromosuccinimide (NBS, 99 %), trimethylamine (TMA) (43.0–49.0 % in water), chlorobenzene (CBN) (ReagentPlus®, 99 %), *N*-methyl-2-pyrrolidone (NMP) (ReagentPlus®, 99 %), methanol (≥99.8 %, ACS reagent), ethyl acetate (EA) (ACS reagent, ≥99.5 %), ammonium hydrogen difluoride (NH_4HF_2) (reagent grade, 95 %) and titanium aluminum carbide (Ti_3AlC_2) (MAX Phase, ≥99.99 %, ≤40 μm particle size) were sourced from Sigma Aldrich, Australia. Platinum on carbon (Pt/C, 46.2 wt%) was procured from Tanaka, Japan, while iridium oxide (IrO_2, 84.5 wt%) was purchased from Alfa Aesar, USA. Fumatech, Germany, supplied the ionomer solution.

2.2. Polymers synthesis

2.2.1. Bromination process

In a three-necked 250 mL glass reactor, 5 g of PPO was dissolved in 86 mL of CBN. The mixture was stirred at 900 rpm at room temperature (RT) under a nitrogen atmosphere in a closed reflux system. The reaction proceeded for 2–3 h until the PPO was completely dissolved. To initiate the bromination reaction, 0.45 mL of AIBN was added to the solution, which was then stirred for 20 min. Subsequently, 3.71 g of NBS was introduced, and the reaction was maintained at 135 °C for 6 h. After completion, the solution was cooled to room temperature and precipitated dropwise into 2 L of methanol using a pipette. The resulting precipitate was magnetically stirred for at least 3 h to ensure thorough washing, followed by vacuum filtration. The washing procedure was repeated at least five times to check the removal of impurities and residual reactants visually. The clean precipitate was dried in a vacuum (0.1 mbar) oven at 60 °C for 12 h. The dried Br-PPO was then collected and stored in a glass bottle with its cap sealed airtight using parafilm tape to prevent exposure to air or moisture, ensuring its stability for subsequent applications.

2.2.2. Quaternization process

To synthesize quaternized PPO (QPPO), 5 g of Br-PPO was dissolved in 95 g of NMP in a 200 mL glass bottle. The mixture was continuously stirred at 60 °C for 3 h until fully dissolved. Next, 7 mL of TMA was added to the solution using a syringe, and the mixture was stirred at RT for 24 h. The resulting solution was precipitated into 1.5 L of EA. The precipitates were washed three times using the vacuum filtration system, following the same procedure as described above. Due to the lightweight nature of the precipitates, careful handling was necessary to avoid adhesion to the filter paper. It was recommended to air-dry the precipitates before collection. The air-dried material was then vacuum-dried at 60 °C overnight. The oven-dried whitish QPPO powder was collected, stored in glass bottles, and preserved for further applications. The polymer synthesis procedures are schematically illustrated in Fig. 2a.

2.3. Synthesis of ammonium hydrogen difluoride (NH_4HF_2)-etched MXene

To synthesize NH_4^+-functionalized MXene, Ti_3AlC_2 MAX powder was etched using NH_4HF_2. Precisely, 10 g of MAX powder was placed in a three-necked flask, and 100 mL of 2 M NH_4HF_2 solution was added. The mixture was continuously stirred at 400 rpm in a closed reflux system at 40 °C for 48 h. After the reaction, the resulting products were thoroughly washed with DI water and centrifuged repeatedly until the pH of the supernatant reached a neutral condition [44,45]. Subsequently, the precipitates were ultrasonically dispersed in DI water for 100 min and

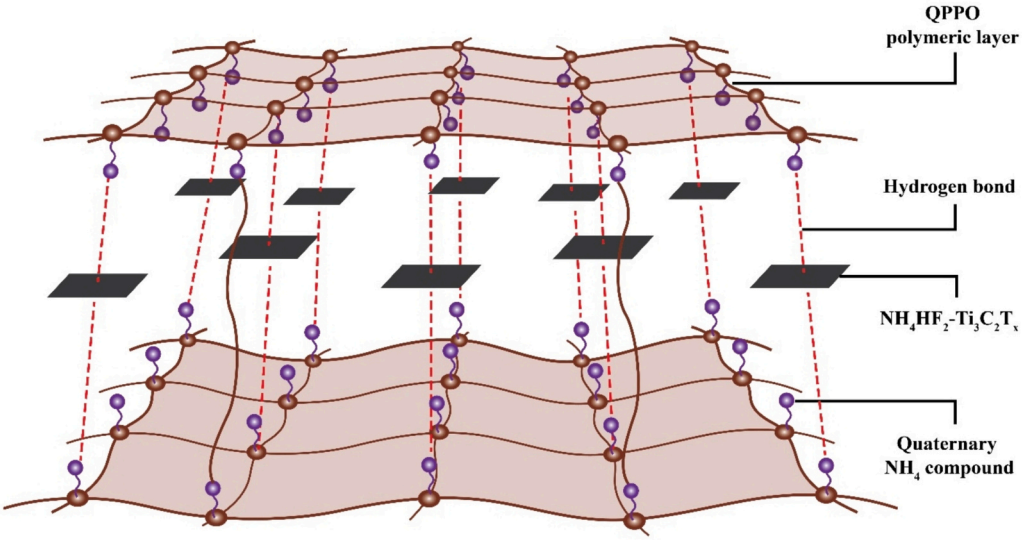

Fig. 1. Schematic illustration of the MXene's role as a reinforcing nano-filler in the QPPO polymer matrix, where interfacial hydrogen-bonding interactions improve compatibility and mechanical stability.

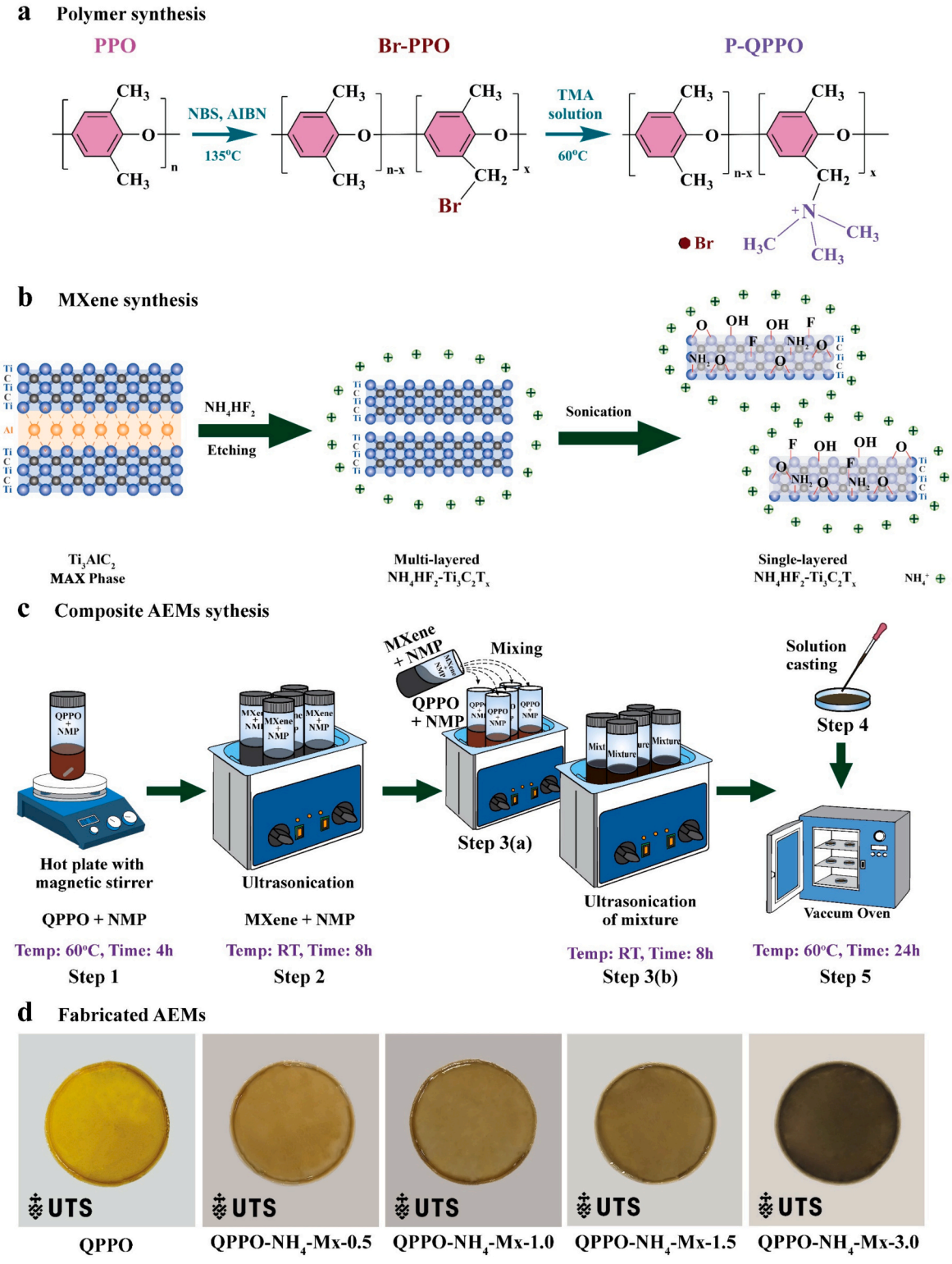

Fig. 2. Schematic illustration of (a) polymer synthesis, (b) MXene synthesis showing the conversion of Ti_3AlC_2 MAX phase into multi-layered and single-layered $Ti_3C_2T_x$ (T_x = -O, -OH, -NH_2, -F) structures through selective etching and sonication steps. The presence of these surface terminations facilitates hydrogen bonding and electrostatic interaction with the QPPO matrix during nanocomposite membrane formation, (c) composite AEMs synthesis procedures and (d) the photographic illustrations of the fabricated AEMs.

centrifuged again to remove any residual contaminations. The collected supernatants were freeze-dried to yield a fluffy black powder of $Ti_3C_2T_x$ MXene, designated as NH_4^+-$Ti_3C_2T_x$. The entire synthesis process was performed in a fume hood, with certain safety precautions. The schematic illustration of NH_4^+-$Ti_3C_2T_x$ synthesis procedures is presented in Fig. 2b.

2.4. Fabrication of QPPO-NH_4-Mx-Y nanocomposite anion exchange membranes (AEMs)

The nanocomposite AEMs were synthesized by reinforcing various weight percentages (0.5–3.0 wt%) of NH_4^+-$Ti_3C_2T_x$ into the QPPO polymer matrix [32]. The role of MXene as a reinforcing filler in the QPPO polymer matrix improves interfacial hydrogen-bonding interactions, increases compatibility and mechanical properties. The detailed fabrication process for a representative AEM with 0.5 wt% NH_4^+-$Ti_3C_2T_x$ (designated as QPPO-NH_4-Mx-0.5) is described below. Initially, 5 mg of MXene and 3 g of NMP were mixed in a glass vial and ultrasonicated for 8 h at RT. Separately, 1 g of QPPO was dissolved in 6 g of NMP in another glass vial, with the mixture heated to 60 °C and stirred for 2–3 h. The two solutions were combined, magnetically stirred for 4 h, and then ultrasonicated for an additional 8 h. The resulting homogeneous solution was filtered with a syringe, cast onto a cleaned glass petri dish, and dried in a vacuum (0.1 mbar) oven at 60 °C for 24 h. The fabricated AEMs were designated as QPPO-NH_4-Mx-Y, where Y indicates the wt% of NH_4^+-$Ti_3C_2T_x$ incorporated. The other membranes, including QPPO-NH_4-Mx-1.0, QPPO-NH_4-Mx-1.5, QPPO-NH_4-Mx-2.0, and QPPO-NH_4-Mx-3.0, were prepared using the same procedure. The schematic illustration of the AEMs fabrication process is shown in Fig. 2c, while their photographic illustration of the is presented in Fig. 2d.

2.5. Materials and AEMs characterization techniques and instrumentation

A comprehensive set of characterization techniques was employed to analyze the physicochemical, structural, and morphological properties of the NH_4^+-$Ti_3C_2T_x$, Br-PPO, QPPO and the composite AEMs. The chemical structures of Br-PPO and QPP were confirmed using ^{1}H NMR spectroscopy on a Bruker AVANCE 600 MHz spectrometer, with deuterated chloroform ($CDCl_3$) as a solvent. FTIR spectra of the samples were recorded using a Bruker VERTEX 70 spectrophotometer equipped with a DTGS detector and a diamond ATR accessory to identify functional groups and confirm chemical modifications. The crystalline structure of NH_4^+-$Ti_3C_2T_x$ was examined using a D8 ADVANCE X-ray diffractometer (Bruker AXS, Germany) with Cu Kα radiation (λ = 1.542 Å), providing insights into the interlayer spacing and structural ordering of the materials. To determine the interlayer properties of NH_4^+-$Ti_3C_2T_x$, HRTEM (FEI Tecnai G2 20 S-Twin) was used. The elemental composition and surface chemical states of NH_4^+-$Ti_3C_2T_x$ were analyzed using an ESCALAB 250Xi spectrometer (Thermo Scientific, UK). Measurements were performed with a 500 μm spot size, 90° photoelectron take-off angle, and pass energies of 100 eV for survey scans and 20 eV for high-resolution scans. Surface and cross-sectional morphologies of the AEMs were observed using FESEM equipped with an energy-dispersive X-ray spectroscopy (EDX) detector. This analysis provided detailed information on membrane thickness, layer integrity, and filler dispersion.

Surface nanostructure and ionic domain morphology of the nanocomposite membranes were assessed by atomic force microscopy (AFM) techniques using a Bruker Dimension Icon system in phase contrast mode. This enabled visualization of microphase-separated hydrophilic and hydrophobic domains, which are critical for ion transport pathways. To support AFM data, the nanoscale structural organization and phase separation behavior of the AEMs were investigated using the small-angle X-ray scattering (SAXS) technique. SAXS measurements were performed on an Anton Paar SAXSPoint 2.0 system (Germany), equipped with a copper microfocus X-ray source (50 kV, 1 mA) and a Dectris Eiger 1M detector, at a sample-to-detector distance (SDD) of 0.557 m. Data were collected under vacuum conditions, with a sample thickness of 40–50 μm and a collection time of 5 min per sample. The SAXS data were processed through azimuthal averaging, binning, and scaling using standard reduction methods. This analysis provided critical insight into the MIPS structure and internal ordering within the membrane matrix, contributing to a deeper understanding of structure-property relationships essential for high-performance AEM design. Measurements were conducted under 25 % relative humidity at RT. The scattering vector (q) was calculated using Eq. (1):

$$q = \frac{4\pi}{\lambda} \times sin2\theta \tag{1}$$

where $\lambda = 1.542$ Å (Cu Kα radiation) and 2θ is the scattering angle. The interdomain spacing (d), representing the average distance between hydrophilic domains, was determined using Eq. (2):

$$d = 2\pi / q_{max} \tag{2}$$

2.6. Dimensional stability measurement of the synthesized AEMs

2.6.1. Determination of ion exchange capacity (IEC)

The IEC of the membranes in their OH^- form was determined using an acid-base back titration method [33]. Prior to the measurement, the Br^- formed membranes were converted into the OH^- form by immersing them in 1 M KOH solution at RT for 24 h. The membranes were then thoroughly rinsed with DI water several times until the washings reached a neutral pH (7), indicating complete removal of excess KOH. After drying the membranes in a vacuum oven at 60 °C overnight, they were accurately weighed (W_{dry}) and immersed in 50.0 mL of a standard 0.01 M HCl solution for 24 h to allow full ion exchange between membrane-bound OH^- groups and Cl^- ions. The remaining HCl in the solution was quantified via titration with 0.01 M NaOH using phenolphthalein as an indicator. A blank titration was also conducted on 10.0 mL of the original 0.01 M HCl solution (without membrane) under identical conditions for comparison. The IEC was calculated using the following expression.

$$IEC\ (mmol/g) = \frac{\left(V_{blank} - V_{sample}\right) \times M_{HCl} \times 1000}{W_{dry}} \tag{3}$$

where V_{blank} and V_{sample} (mL) are the volumes of 0.01 M NaOH required to titrate 10.0 mL of HCl solution for the blank and membrane-treated samples, respectively. M_{HCl} is the molarity of HCl (0.01 mol/L). W_{dry} is the dry mass of the membrane sample (g), and the factor 1000 converts moles to millimoles. All measurements were performed in triplicate to ensure accuracy and reproducibility, and the average IEC values were reported.

2.6.2. Water uptake (WU) and swelling ratio (SWR) of AEMs

The WU and SWR of the AEMs in their OH^- form were determined by measuring the changes in weight/dimensions of the membrane samples. The membranes were immersed in DI water at RT for 48 h to reach water absorption equilibrium. After removing excess water using tissue paper, the fully hydrated membranes were weighed immediately (M_{wet}). The samples were then dried under vacuum at 60 °C until a constant weight was achieved (M_{dry}). The water uptake was calculated using Eq. (4):

$$WU\ (\%) = \frac{M_{wet} - M_{dry}}{M_{dry}} \times 100 \tag{4}$$

Likewise, the area and thickness of the membranes were measured before and after hydration to calculate the SWR in volume, using Eq. (4):

$$SWR\ (\%) = \frac{V_{wet} - V_{dry}}{V_{dry}} \times 100 \tag{5}$$

where V_{wet} and V_{dry} represent the volume of the membranes in the wet and dry states, respectively.

2.7. Electrochemical, mechanical and thermal properties of the AEMs

2.7.1. Ion conductivity (IC)

To determine the OH^- IC of AEMs, they were initially wet in a 1 M KOH solution for 24 h to replace the bromide (Br^-) ions with OH^- ions. Following the ion exchange, the membranes were thoroughly rinsed with DI water until the solution reached a neutral pH, ensuring the removal of excess KOH. The membrane resistance (R) was measured in DI water using EIS techniques with a customized 4-probe IC cell (CNL Energy, Republic of Korea), equipped with platinum wire electrodes spaced 0.5 cm apart. The set-up was connected to a Biologic SP-200 potentiostat (Bio-logic science instruments, France), and measurements were conducted in galvanostatic EIS (GEIS) mode via EC-Lab software. The alternating current frequency ranged from 100 kHz to 100 MHz.

$$\sigma\ (mS\ cm^{-1}) = \frac{L}{R.A} \tag{6}$$

Here, R represents the resistance (Ω) of the membrane, L (cm) denotes the distance between the two platinum electrodes, and A indicates the cross-sectional area through which current flows (cm^2).

2.7.2. Measurement of alkaline stability of the composite AEMs

The alkaline stability of the AEMs was evaluated by immersing the membranes in 1 M KOH solution at 60 °C for up to 504 h, while periodically monitoring changes in IC. After each stability interval, the membranes were thoroughly rinsed with DI water until the rinsed solution reached neutral pH to ensure complete removal of excess KOH. Subsequently, the OH^- IC of the membranes was determined following the procedure described in Section 2.7.1.

2.7.3. Mechanical and thermal integrity of the composite AEMs

The tensile strength (TS) of the AEMs was evaluated with a universal tensile strength testing instrument (SANS CMT6502) operated at a stretching rate of 5 mm min^{-1}. The membrane samples were cut into dumbbell-shaped specimens with dimensions of 4 mm in width and 25 mm in length prior to testing. The thermal strength of the AEMs was investigated by TGA analysis using an HT/808 instrument (METTLER TOLEDO, Greifensee, Canton Zurich). Measurements were carried out under a nitrogen (N_2) atmosphere at a heating rate of 10 °C min^{-1} with a temperature range of 0–700 °C.

2.8. Preparation of membrane electrode assemblies (MEAs)

To evaluate the performance of the synthesized AEMs, membrane electrode assemblies (MEAs) were fabricated. The cathode utilized Pt/C as the catalyst, while IrO_2 was employed as the anode catalyst. Catalyst inks were prepared by dispersing the respective catalysts and ionomer solution in isopropyl alcohol (IPA) through ultrasonication to achieve a homogeneous mixture. The MEAs were assembled using the catalyst-coated substrate (CCS) [14] technique, ensuring uniform application of the catalyst layers and optimal integration with the AEMs for enhanced performance. The anode was coated with 2.0 mg cm^{-2} of IrO_2, while the cathode was loaded with 0.4 mg cm^{-2} of Pt/C.

2.9. Electrolysis cell performances of the nanocomposite AEMs

The cell performance of QPPO-NH_4-Mx-3.0 AEM, optimized for OH^- IC and alkaline stability, was evaluated using an alkaline water electrolysis test station (CNL Energy, Korea). The membrane electrode assembly (MEA) was configured in a sandwich arrangement, incorporating the AEM, gas diffusion layer (GDL), and gasket (Fig. 3). Single-cell testing was conducted with an effective electrode area of 25 cm^2. The system employed 0.1 M and 1 M KOH solutions as feed electrolytes, supplied at a flow rate of 50 mL min^{-1}. The cell was operated at a temperature of 60 °C. Water electrolysis performance was measured in a liquid-fed configuration, with a continuous water supply at the anode. The relative humidity (70–96 %) indicates the controlled gas-phase humidity at the cathode side, which was used to maintain membrane hydration during the tests. The current density was recorded as the cell voltage was varied from 1.4 to 2.0 V. Lab-scale durability testing was performed using an impedance analyzer (ZIVE MP5, WonATech, Korea) under constant current densities of 0.5 and 1.0 A cm^{-2}. Corresponding voltages were recorded over a 150-h operational period to assess the long-term stability of the cell.

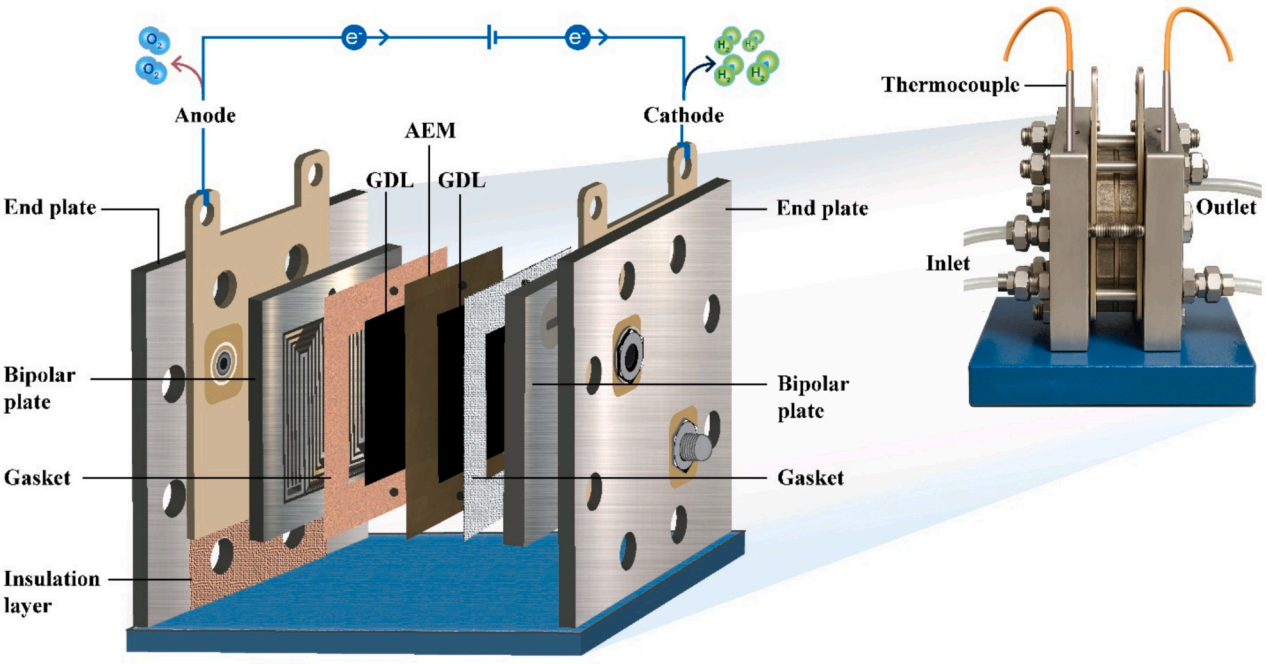

Fig. 3. Schematic of the AEMWE cell. The end and bipolar plates are made of stainless steel, while the electrodes are made up of gold-coated copper. The AEM was sandwiched in between GDL and gaskets. The effective electrode area of the cell was 25 cm^2.

3. Results and discussion

3.1. MXene and polymer characterization

3.1.1. Morphology, structural and surface functionalities of MXene

The chemical structure of single-layer NH_4^+-$Ti_3C_2T_x$ in this study has been presented in Fig. 4. The FESEM micrograph and EDX elemental mapping of the functionalized MXene have been provided in Fig. 5. The FESEM micrograph reveals a layered and crumpled morphology, characteristic of exfoliated MXene. Compared to the parent MAX phase, the structure appears delaminated, with thin, wrinkled and accordion-like sheets (Fig. 5a). This indicates successful etching and exfoliation, likely increasing surface area [34].

The absence of large, intact MAX-like structures confirms the removal of A-site elements (e.g., Al) [35]. Additionally, some restacking is visible, which can occur during drying or due to interlayer interactions after NH_4^+ functionalization. Such partial restacking is commonly observed in functionalized MXene and is not inherently detrimental. While excessive restacking can reduce accessible surface area and limit the availability of ion-conducting functional groups, a moderate degree of sheet overlap may increase structural stability within the MXene-polymer matrix interface. This balance can be beneficial for nanocomposite membranes, as it mitigates the risk of excessive swelling while still preserving adequate ion transport pathways.

The open and porous nature suggests that functional groups, including NH_4^+, may have intercalated, leading to possible structural expansion [36]. Ti is evenly distributed, confirming that the MXene phase is preserved after functionalization (Fig. 5b). The presence of Ti-rich areas correlates with the FESEM image, where the MXene flakes dominate the field of view [37]. The carbon distribution appears non-uniform since MXene is a Ti-C-based material; a stronger C signal in well-exfoliated areas would be expected (Fig. 5c).

The relatively weaker and non-uniform C signal, despite MXene being a Ti-C-based material, can be attributed to the well-known limitations of EDX analysis. Because Ti has a higher atomic number and stronger backscattering effect, it dominates elemental contrast and often obscures lighter elements such as C. Moreover, the abundance of surface terminations (-O, -OH, -F, $-NH_2$) further attenuates C detection in the near-surface region. Consequently, the observed carbon distribution does not indicate true compositional heterogeneity or processing variability but rather reflects intrinsic measurement sensitivity and surface functionalization effects. In contrast, Ti mapping appears uniform owing to its inherently stronger detectability in EDX. Oxygen is not homogeneously distributed, forming localized clusters recommended surface oxidation and the presence of hydroxyl (-OH) groups from synthesis or NH_4^+ exchange reactions (Fig. 5d). The presence of F indicates residual -F terminations, which are common in NH_4^+-etched MXene [38]. Since $-NH_4^+$ functionalization is expected to replace some F groups, the remaining F suggests partial functionalization rather than complete exchange (Fig. 5e). N is clearly detected, confirming the presence of NH_4^+ groups. The dispersed pattern suggests successful functionalization, though it is not completely uniform (Fig. 5f). This could be due to the partial replacement of -F or -OH groups by NH_4^+ [39].

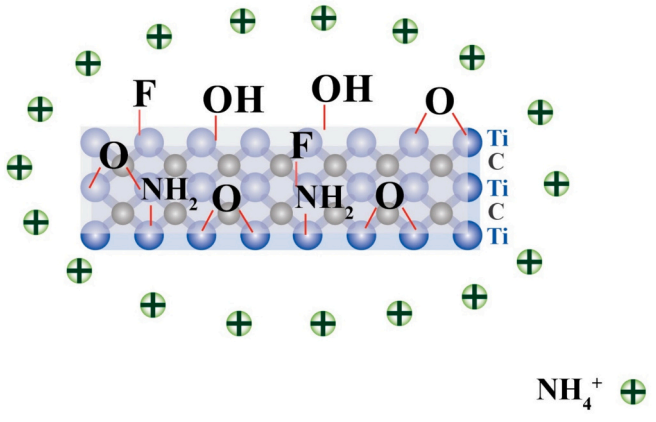

Fig. 4. Schematic illustration of the chemical structure of single-layer NH_4^+-$Ti_3C_2T_x$ used in this study, showing typical surface terminations (T_x = -O, -OH, -F, and $-NH_2$). The surface functional groups originate from the NH_4HF_2 etching process and play a critical role in enhancing hydrophilicity and interfacial interactions with the QPPO matrix.

The FTIR and XRD analyses were conducted to gain insights into the structural and chemical properties of the synthesized NH_4^+-$Ti_3C_2T_x$ [40,41]. The FTIR spectra reveal significant changes in surface functional groups following functionalization. A strong N—H peak at 2988 cm^{-1} confirms successful NH_4^+ incorporation, while the broad O—H stretching peak at 3673 cm^{-1} (Fig. 6a) reflects enhanced hydrophilicity, crucial for improved water interaction and ion transport properties [41]. The C═C peak at 800 cm^{-1} confirms the preservation of the MXene backbone structure during functionalization. The XRD spectra, illustrated in Fig. 6b, further substantiate the impact of functionalization on the NH_4^+-$Ti_3C_2T_x$ structure. The peak at $2\theta = 43.8°$, associated with residual Al layers in the Ti_3AlC_2 MAX phase, diminishes or disappears in NH_4^+-$Ti_3C_2T_x$, indicating successful Al removal during the etching process, which has already been validated by previous publications [42–45]. The emergence of a prominent peak at $2\theta = 6.28°$ in NH_4^+-$Ti_3C_2T_x$ confirms NH_4^+ intercalation, which expands the interlayer spacing. This shift to lower angles highlights structural expansion due to $-NH_4^+$ group insertion, facilitating ion transport and reducing ohmic resistance, thereby enhancing electrochemical efficiency [46].

Transmission electron microscopy (TEM) provided direct evidence of the morphology of the synthesized MXene. As shown in Fig. 6d, the nanosheets exhibit a flake-like layered structure typical of two-dimensional MXene materials. The sheets are thin and highly transparent, with lateral dimensions predominantly in the range of 200–500 nm, although smaller fragmented domains (<50 nm) are also occasionally observed, likely due to sonication during the delamination process. The contrast variation in the TEM images suggests the coexistence of few-layer regions and partially restacked domains, indicating successful exfoliation but with some degree of aggregation. The edges of the nanosheets appear sharp and well defined, further confirming the 2D morphology. The TEM observations, together with the characteristic peaks identified in XRD and the complementary FESEM analyses, confirm the successful preparation of two-dimensional MXene nanosheets. The thin-layered morphology is particularly important for their role as reinforcing fillers in the QPPO polymer matrix, as the high aspect ratio and strong interfacial interactions are expected to facilitate improved dispersion, enhanced mechanical stability, and more efficient ionic transport in the resulting membranes.

The wide-scan XPS spectrum confirms the presence of C, O, Ti, N, and F elements in the material, as indicated by the characteristic peaks for C 1s, O 1s, Ti 2p, N 1s, and F 1s. Minor signals from Al species are also detected, possibly originating from the substrate or residual precursor (Fig. 7a). The high-resolution Ti 2p profile shows prominent peaks at 458.6 eV and 464.3 eV, corresponding to Ti $2p_{3/2}$ and Ti $2p_{1/2}$ of TiO_2, confirming the presence of oxidized titanium. Additional peaks at 456.7 eV and 462.4 eV correspond to Ti^{2+} species, while low binding energy components indicate Ti—C bonding, suggesting partial incorporation of Ti into carbide phases (Fig. 7b). The deconvoluted C 1s spectrum displays peaks for O—C═O (289.1 eV), C═O (287.1 eV), C═C (284.7 eV), C—O (285.6 eV), Ti—C—Ti (282.1 eV), and Ti═C (281.5 eV). The strong sp^2 carbon peak (C═C) indicates graphitic domains, while the Ti—C related signals confirm the formation of titanium carbide (Fig. 7c). The oxygen spectrum contains peaks at 530.1 eV (C═O), 531.2 eV (C—O), and 532.3 eV (C-Ti-O), indicating the coexistence of oxygen in both organic and inorganic coordination environments. The C-Ti-O feature supports surface oxidation of Ti-C sites (Fig. 7d). The F 1s region shows a dominant peak at 685.1 eV attributed to C—Ti—F, and a smaller

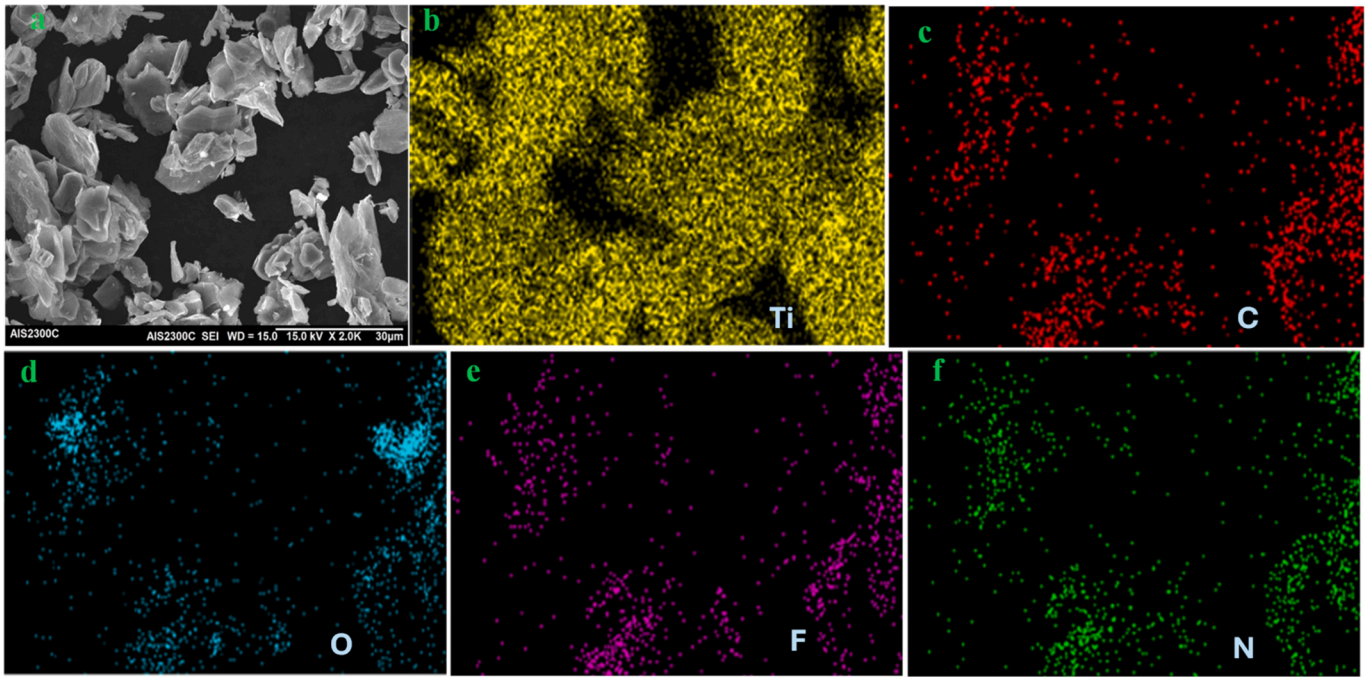

Fig. 5. (a) FESEM micrograph of NH_4^+-$Ti_3C_2T_x$ MXene, (b-e) EDX elemental composition of NH_4^+-$Ti_3C_2T_x$ MXene.

contribution at 687.2 eV corresponding to Al (OF)x species, likely originating from etching agents during synthesis (Fig. 7e). Two major peaks at 400.6 eV (N—C) and 398.9 eV (N—Ti—O) indicate nitrogen incorporation into both carbonaceous domains and Ti—O—N configurations, suggesting surface doping or nitrogen functionalization (Fig. 7f). Overall, the XPS results confirm the successful formation of a multi-element MXene material with Ti—C, Ti—O, and Ti—F bonds, along with nitrogen functionalities originated from NH_4^+ groups, which may synergistically contribute to the desired surface and catalytic properties in the synthesized AEMs.

3.2. Structural transformation of PPO via bromination and quaternization

The structural modifications of PPO through bromination and subsequent quaternization were analyzed using ^{1}H NMR spectroscopy, as shown in Fig. 8a–b. In Br-PPO, the aromatic protons exhibited chemical shifts between 6.3 and 6.6 ppm, while the benzylic protons (-CH_2Br) appeared at 4.3 ppm, confirming bromination at the benzylic position [47]. Additionally, the methyl protons attached to the aromatic ring showed a sharp signal at 1.45 ppm [48]. Upon quaternization, the disappearance of the -CH_2Br peak and a shift of the aromatic protons to 6.5–6.9 ppm indicates the substitution of bromide with quaternary ammonium groups. The benzylic protons (-CH_2) remained at 4.3 ppm, while a new peak at 3.3 ppm corresponds to the *N*-methyl protons, further confirming the quaternization process [48]. Furthermore, the methyl protons associated with the nitrogen centre were observed at 2.0 ppm, providing additional evidence for the successful formation of quaternary ammonium groups. Further evidence of the chemical transformations in brominated and quaternized PPO was obtained through FTIR spectroscopy, as shown in Fig. 6c. The chemical shifts and assignments of protons in Br-PPO and QPPO have been presented in Table 1.

The FTIR spectra of Br-PPO and QPPO revealed distinct structural modifications while maintaining the overall integrity of the polymer backbones. The FTIR analysis is based on qualitative peak assignment rather than quantitative deconvolution of peak intensities. The characteristic peaks at 2900 cm^{-1} for C—H stretching, 1600 cm^{-1} for aromatic C═C stretching, and 1250–1180 cm^{-1} for C—O—C ether vibrations confirmed the fundamental structure of the PPO backbone. In Br-PPO, the presence of peaks at 588.2 and 782.8 cm^{-1}, corresponding to C—Br stretching, provided clear evidence of successful bromination [49]. However, a weak absorption band observed around 3500–3600 cm^{-1} in the FTIR spectrum of Br-PPO can be attributed to trace —OH stretching vibrations. This feature likely arises from physically adsorbed moisture on the polymer surface or minor hydroxylated species formed during bromination. The presence of polar C—Br bonds may facilitate slight water adsorption, while incomplete drying or side reactions under bromination conditions could also contribute to the appearance of this band. In QPPO, the disappearance of the C—Br peaks, coupled with the emergence of new peaks between 900 and 1200 cm^{-1} associated with C—N and N—CH_3 stretching, confirmed the successful quaternization of PPO [50]. These spectral transitions align closely with the structural insights derived from ^{1}H NMR analysis (Fig. 8), providing a comprehensive validation of the bromination and quaternization processes of the polymers. Taken together, the NMR and FTIR data consistently confirm successful quaternization that enhances the hydrophilicity of the polymer, which is expected to enable the construction of continuous ionic channels and improve OH^- ion transportation in the nanocomposite AEMs.

3.3. Characterization of the nanocomposite AEMs

3.3.1. Morphology

The morphological characteristics of the pristine QPPO and nanocomposite AEMs are illustrated in Fig. 9. It is worth noting that the thickness of the membranes varied from 40 to 50 μm. The FESEM micrographs reveal that the surfaces and cross-sections of the AEMs are densely smooth and devoid of significant agglomeration or defects. This observation indicates a homogeneous dispersion of MXene and strong compatibility between MXene and the QPPO matrix. Notably, as the weight percentage (wt%) of MXene increases, the overall surface roughness of the AEMs also increases. This can be attributed to the fact that as the wt% becomes higher, more Mxene are deposited on the surface, and thus the surface roughness increases [51,52]. Additionally, higher MXene loadings could cause micro or nano-scale protrusions on

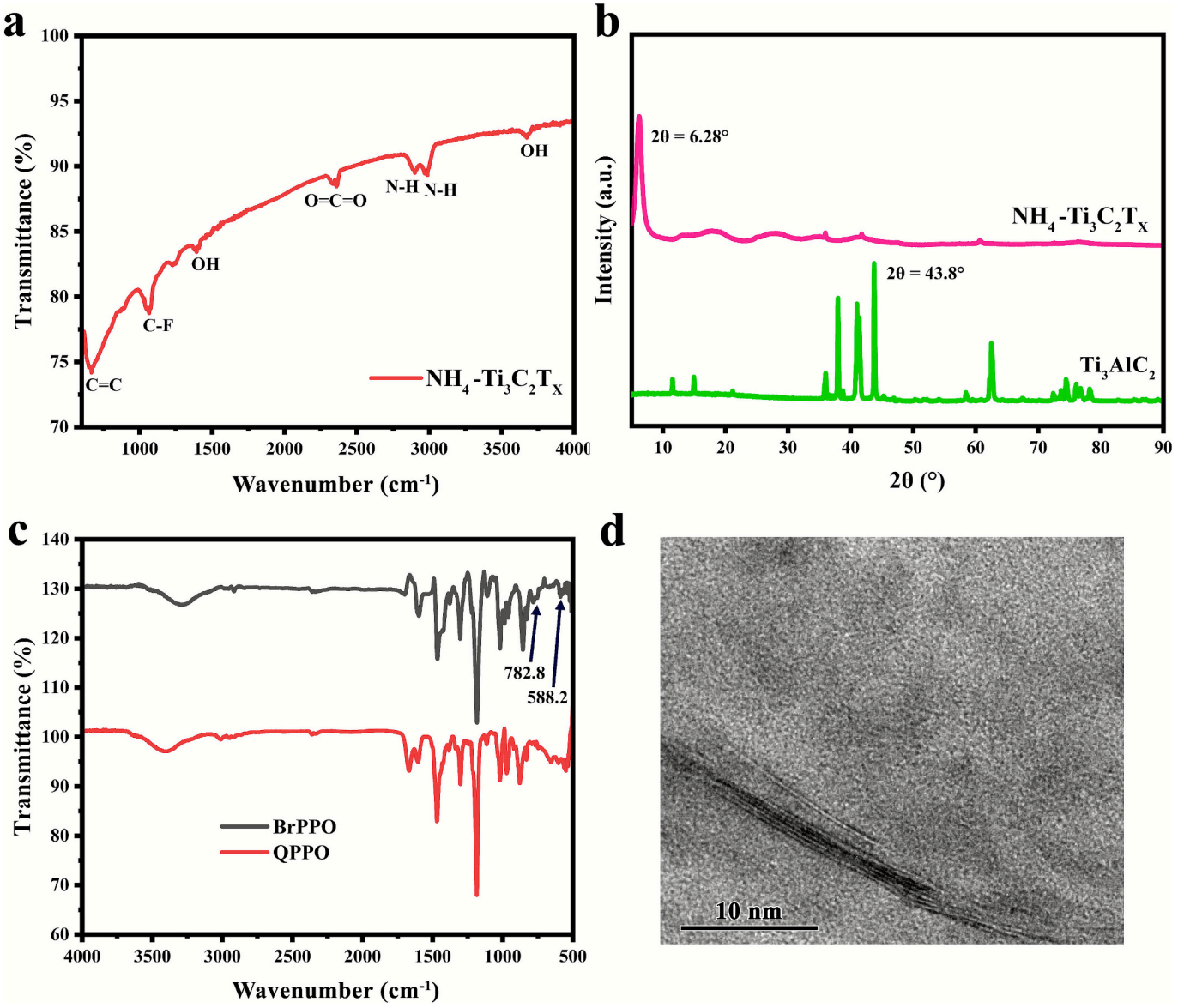

Fig. 6. Characterization of polymers and MXene; a) FTIR spectra of MXene, b) XRD spectra of MXene [44,45], c) FTIR spectra of Br-PPO and QPPO and d) HRTEM of NH_4^+-$Ti_3C_2T_x$.

the membrane surface, increasing the roughness (Fig. 9) [53].

Increased surface roughness can positively influence membrane performance by enhancing the effective surface area, which facilitates hydroxide ion transport through improved access to hydrophilic pathways. Moreover, rougher surfaces may improve wettability, promoting better interaction between the membrane and aqueous electrolytes. However, excessive roughness could also potentially increase the risk of fouling or localized stress points, highlighting the importance of optimizing MXene content for a balanced performance. EDX spectra in Fig. 9 (g) provide complementary insights into the elemental composition of the QPPO-NH4-Mx-3.0 wt% composite AEM, which serves as a representative of all fabricated AEMs. The EDX results affirm the effective integration of MXene into the polymer matrix, aligning with the FESEM observations.

The high carbon content originates from both the QPPO matrix and MXene, reflecting their significant structural contributions, whereas oxygen (19.50 %) is derived from the QPPO backbone and surface functional groups (-O, -F, and -OH and -NH_2) of MXene, highlighting strong polymer-additive interactions. Titanium (21.91 %), which is one of the core components of MXene confirmed the successful incorporation of MXene into the polymer matrix. Nitrogen (3.03 %) arises from ammonium functionalization, enhancing the hydrophilicity and ion transport properties of the AEMs [54]. These measured elemental compositions are generally consistent with the theoretical expectations for a 3 wt% MXene loading, indicating that the MXene is well-dispersed within the QPPO matrix. Fluorine, along with oxygen, supports the chemical integrity of the MXene and validates their integration into the AEMs. These results confirm the structural and compositional robustness of the nanocomposite AEMs, with the inclusion of MXene contributing to enhanced ion transport and hydrophilic properties.

In essence, based on the FESEM-EDX analysis, it is well evident that although slight surface inhomogeneity can be seen at higher MXene loadings, this is attributed to minor restacking of MXene sheets and does not form through-thickness defects or affect the membrane's structural integrity. Furthermore, the cross-sectional FESEM image confirms a compact and uniform architecture (49.99 μm thickness), while the EDX spectrum verifies the homogeneous presence of C, O, N, F, and Ti elements throughout the membranes. These results collectively demonstrate that the incorporation of MXene does not compromise membrane

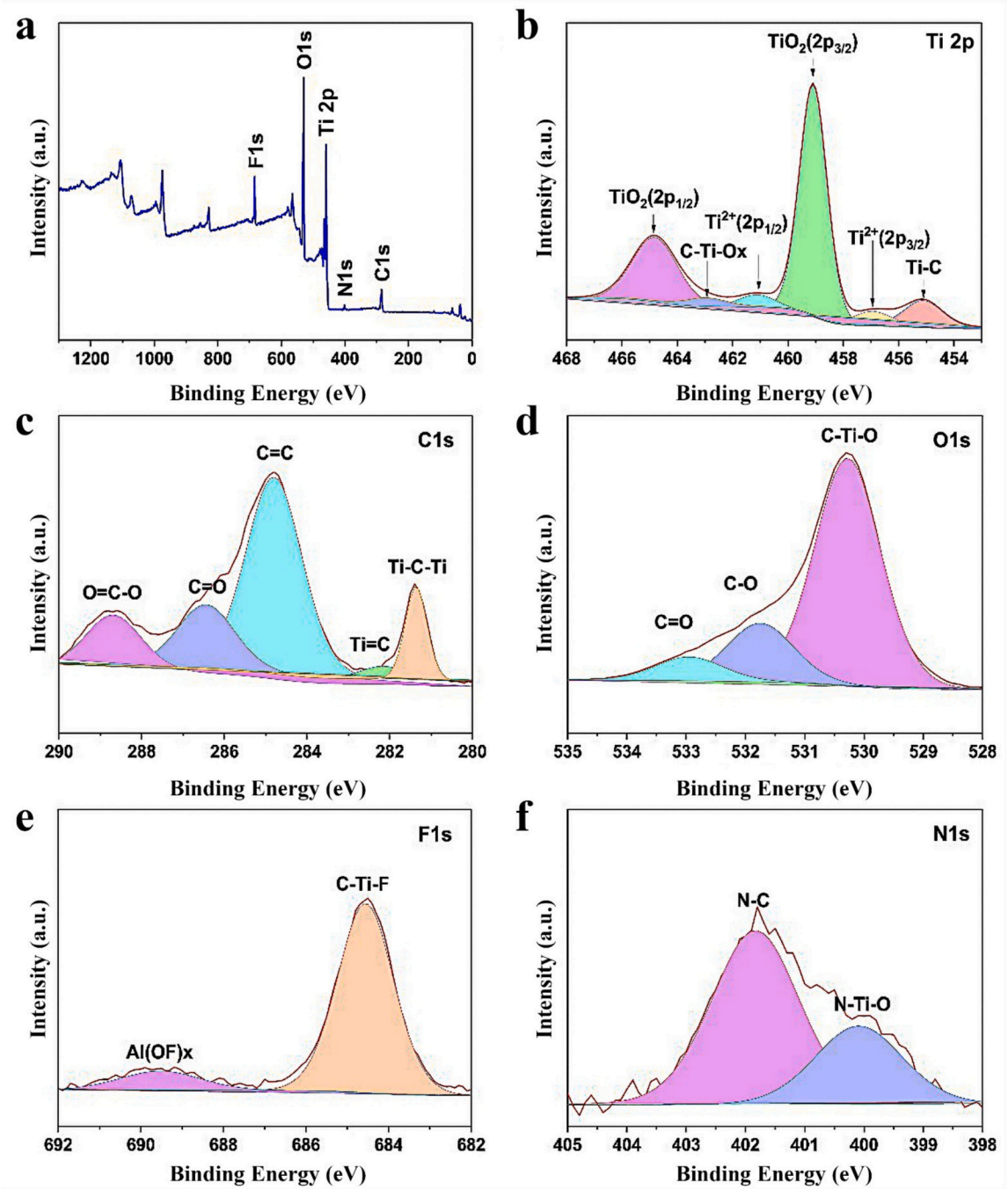

Fig. 7. (a) Wide-scan XPS spectrum of NH_4^+-$Ti_3C_2T_x$ and XPS fitting curves of Ti 2p (b), C 1s (c), O 1s (d), F 1s (e) and N1s (f).

density or integrity. On the contrary, MXene's two-dimensional layered structure is known to act as a barrier-type additive, increasing the tortuosity of diffusion pathways. This characteristic is expected to reduce, rather than increase, gas permeability. The stable electrolysis performance observed in our study further supports that no detrimental gas crossover or leakage occurred under the specified operating conditions.

3.3.2. *Dimensional and mechanical stability of the nanocomposite AEMs*

In the development of alkaline AEMs, achieving an optimal balance among WU, ion IEC, and mechanical stability is crucial. Water content in AEMs plays a pivotal role in forming hydrated ionic phase domains, which are essential for efficient ion transport, particularly for OH^- ions. However, excessive WU can lead to undesirable membrane expansion, resulting in reduced mechanical strength and an increased SWR. These effects compromise membrane durability and performance. Therefore, maintaining these properties within reasonable limits is vital to ensure both high IC and mechanical robustness [55,56]. PPO-based membranes are known to exhibit high WU, SWR, and IEC, which contribute to their electrochemical performances. However, these properties often compromise mechanical integrity, limiting the long-term durability and operational stability of such membranes in the WE process [57,58]. Optimizing WU and IEC while maintaining mechanical stability is crucial for reliable AEM performance in alkaline water electrolysis.

The dimensional and mechanical properties of the AEMs are illustrated in Fig. 10. The data reveal that increasing temperature (30–80 °C) leads to higher WU (%) and SWR (%) (Figs. 10a–b. However, increasing the wt% of NH_4^+-$Ti_2C_3T_x$ in the membranes results in a decrease in these properties. This behavior can be attributed to the hydrophilic functional

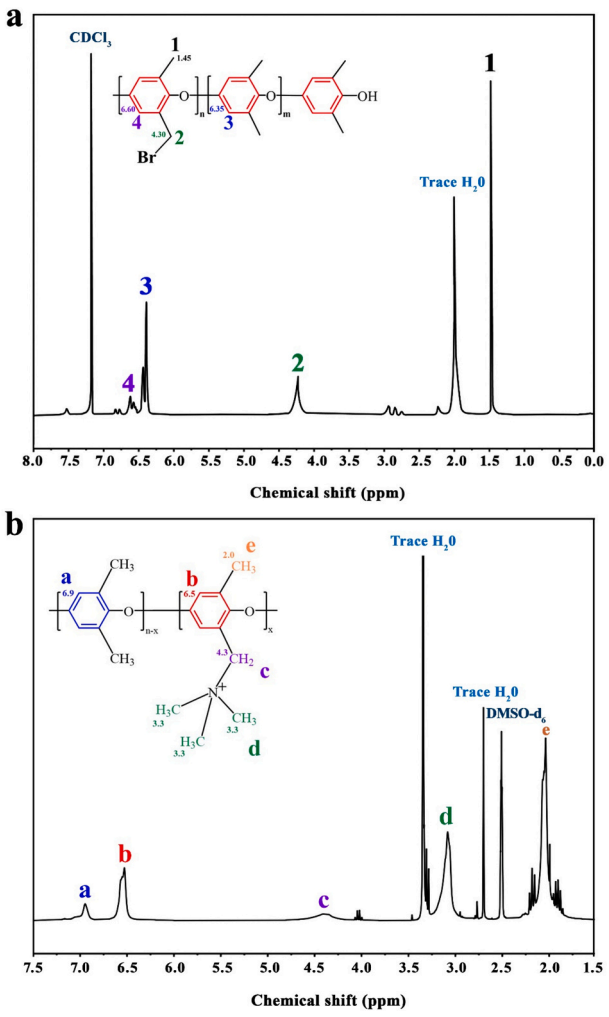

Fig. 8. ^{1}H NMR spectra of Br-PPO(a), ^{1}H NMR spectra of QPPO (b).

Table 1
Summary of ^{1}H NMR chemical shifts and proton assignments for Br-PPO and QPPO.

δ (ppm)	Assignment	Structural groups
6.3–6.6	Aromatic H	Aromatic protons in Br-PPO
4.3	Benzylic H	-CH_2Br group in Br-PPO (disappears after quaternization); -CH_2 adjacent to quaternary ammonium in QPPO
1.45	Methyl H	-CH_3 group attached to aromatic ring
6.5–6.9	Aromatic H	Aromatic protons shifted after quaternization (QPPO)
3.3	N–CH_3 H	*N*-methyl protons (new peak after quaternization)
2.0	Methyl H	Methyl protons associated with nitrogen centre (quaternary ammonium)

groups (-OH, -O, -F, and -NH_2) present on the surface of MXene, which interact with water molecules. At higher MXene loadings, these functional groups bind more strongly to water, reducing the availability of free water for bulk hydration. Consequently, WU and SWR are limited [59]. Although MXene is hydrophilic, the water it binds is more tightly associated with surface functional groups, limiting free water for swelling. Additionally, the layered structure of MXene physically restricts expansion, collectively reducing excessive membrane swelling.

Additionally, excessive MXene loading may disrupt the formation of well-connected, hydrated ionic phase domains within the polymer matrix. This disruption hinders the development of effective water transport pathways, further reducing the membrane's capacity to absorb and retain water [60,61]. Nonetheless, the composite AEMs exhibited controlled WU and SWR, ranging from 17.8 to 36.2 % and 6.5–16.2 %, respectively, significantly lower than those of the pristine QPPO membrane. The pristine QPPO membrane exhibited the lowest IEC of 2.09 mmol g^{-1}. The incorporation of MXene into the QPPO matrix led to a slight increase in IEC, ranging from 2.09 to 2.52 mmol g^{-1} as the MXene content increased up to 3 wt% (Fig. 10c), while the QPPO-NH_4-Mx-3 demonstrated a maximum IEC of 2.52 mmol g^{-1}. The increasing MXene content enhances IEC due to the introduction of more ion-exchange sites, due to their abundant surface functionalities (e.g., -OH, -F, -O and -NH_2) [59]. Moreover, the large surface area of MXene provides more active sites for ion exchange. Furthermore, MXene also improves the distribution of functional groups and connectivity between ion exchange sites [62].

The hydrophilic nature of MXene facilitates better ion mobility [63], and the interaction between MXene and the polymer matrix creates more efficient ion transport pathways, collectively contributing to higher IEC and improved membrane performance. [64]. It should be noted that MXene itself does not act as a traditional ionomer; rather, its large surface area and strong interactions with QPPO improve the dispersion and connectivity of the polymer's quaternary NH_4^+ groups, effectively enhancing the membrane's IEC. These effects are confirmed by the lower WU and SWR values observed for the composite AEMs compared to the pristine QPPO membrane.

The TS of the AEMs ranged from 15.2 to 61.2 MPa (Fig. 10d), with the maximum TS recorded for QPPO-NH_4-Mx-3.0 at 61.2 MPa. The increase in TS with higher MXene content can be attributed to MXenes' two-dimensional structure, high mechanical strength, and stiffness, which enable them to act as reinforcing fillers. When dispersed within the membrane matrix, MXene provides structural support, significantly enhancing the overall mechanical properties of the composite membrane. Furthermore, MXene forms strong interactions with the polymer matrix through mechanisms such as hydrogen bonding, electrostatic interactions, or van der Waals forces [65,66].

These interactions facilitate efficient stress transfer from the polymer matrix to the MXene particles, thereby contributing to the observed improvement in TS. However, Fig. 10d also shows that the elongation at break (EB) of the nanocomposite AEMs decreased with increasing MXene content. This reduction in EB can be explained by the restricted mobility of polymer chains caused by the presence of MXene particles, which act as physical barriers. The diminished chain mobility reduces the material's ability to stretch, leading to a lower elongation at break [67–69]. Commercial AEMs typically exhibit IEC ranging from 1.5 to 2.5 mmol g^{-1} and tensile strength (TS) between 40 and 60 MPa [13]. In essence, the QPPPO-NH_4-Mx-3.0 strikes an optimal performance based on the dimensional and mechanical performances of the synthesized AEMs by minimizing the trade-off interactions among those properties.

Although the elongation at break of the membranes decreased progressively with increasing MXene content, indicating reduced flexibility due to restricted polymer chain mobility caused by the rigid two-dimensional MXene sheets. This trend is typical in polymer-nanofiller composites, where strong interfacial interactions (e.g., hydrogen bonding) and physical entanglement between the filler and polymer backbone limit chain deformation under stress. Despite the lower elongation, the tensile strength (61.2 MPa) of QPPO-NH_4-Mx-3.0 was substantially enhanced compared to pristine QPPO, confirming the reinforcing effect of MXene. The concurrently low swelling ratio (10.5 %) further verified improved dimensional stability and compact structural organization. Such characteristics are particularly desirable for AEMWE operation, where mechanical strength and dimensional integrity are more critical than high ductility, as the membranes are clamped between electrodes and operate under minimal strain. Therefore, the observed reduction in elongation is considered an acceptable trade-off for achieving enhanced rigidity, anti-swelling capacity, and long-term operational stability. Moving forward, further improvement in flexibility and mechanical resilience could be achieved through surface

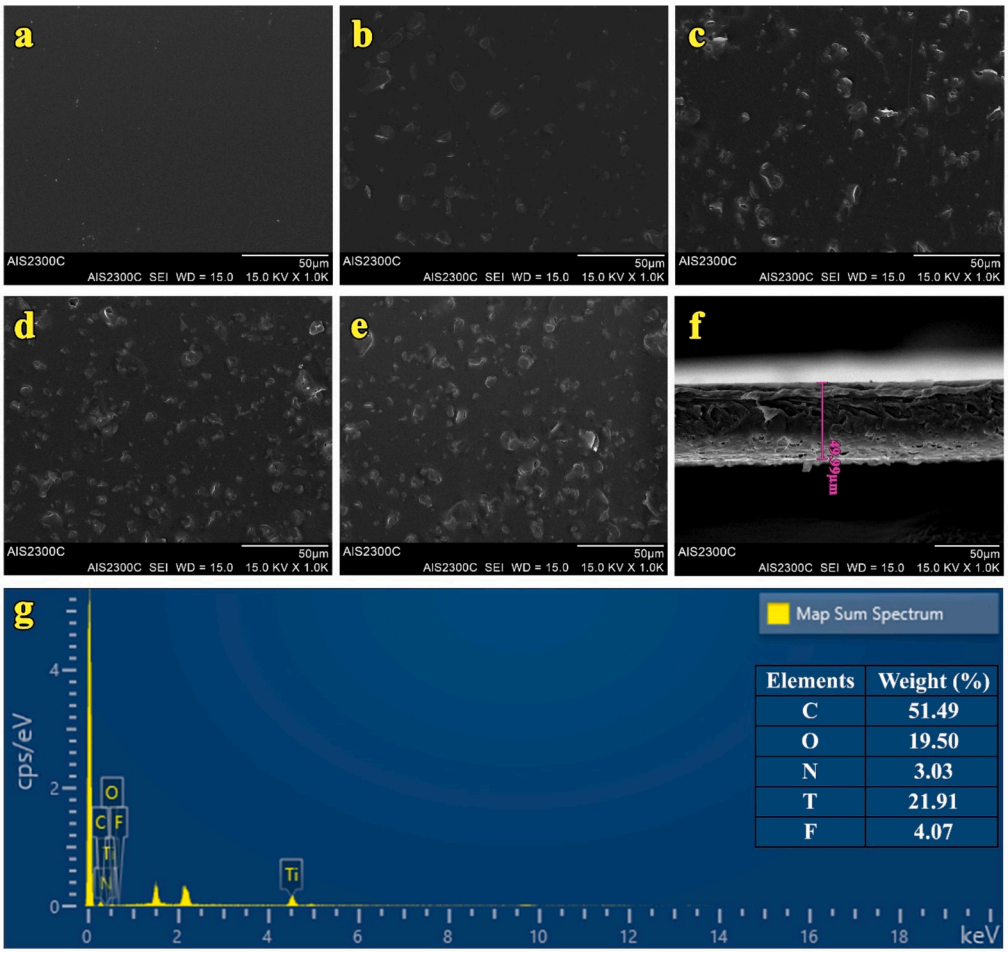

Fig. 9. FESEM micrographs of (a) Pristine QPPO; (b) QPPO-NH_4-Mx-0.5; (c) QPPO-NH_4-Mx-1.0; (d) QPPO-NH_4-Mx-1.5; (e) QPPO-NH_4-Mx-3.0; (f) Cross section of QPPO-NH_4-Mx-3.0 and (g) EDX spectra of QPPO-NH_4-Mx-3.0.

modification of MXene to improve interfacial compatibility, copolymer toughening to enhance matrix elasticity, and incorporation of flexible crosslinkers such as SEBES or Bis[2-(*N*,*N*-dimethylamino)ethyl] ether (BDME) to create a more compliant yet mechanically robust network [70].

3.3.3. *Hydroxide ion conductivity and phase-separation structures of the nanocomposite AEMs*

The incorporation of NH_4^+-$Ti_2C_3T_x$ into the QPPO polymer matrix significantly reduces water WU and SWR, as shown in Fig. 10a–b. This enhancement also improves the mechanical stability of the AEMs, as illustrated in Fig. 10d. Additionally, the IC of the composite AEMs is enhanced, as presented in Fig. 11c–d. These improvements result from the formation of a microphase-separated structure due to interactions between the hydrophilic MXene and the hydrophobic QPPO polymer matrix [71–73]. AFM micrographs offer valuable insights into the microphase separation, revealing distinct hydrophilic and hydrophobic regions within the membranes.

For example, the pristine QPPO membrane (Fig. 11a) exhibits a smooth and homogeneous surface, indicating the absence or less of phase separation morphologies. In contrast, the QPPO-NH_4-Mx-3.0 AEM (Fig. 11b) shows well-defined microphase-separated domains formed by the uniform dispersion of NH_4^+-$Ti_2C_3T_x$. These domains establish continuous hydrophilic pathways that facilitate ion conduction through functional groups (-O, -OH, -F and -NH_2) on the MXene surface while preserving the dimensional and mechanical stability of the composite AEMs [54]. In particular, the -O, -OH, and -F and -NH_2 groups on MXene interact with water molecules, promoting water structuring and facilitating OH^- ion dissociation. Thus, the enhanced OH^- conductivity results from both the microphase-separated morphology and the chemical activity of MXene's surface functionalities, rather than from MXene acting merely as a passive filler.

The data in Fig. 11c demonstrates a strong positive correlation between OH^- IC, temperature, and MXene content. Among the tested AEMs, QPPO-NH_4-Mx-3.0 exhibits exceptional performance, achieving an IC of 153.2 mS cm^{-1} at 80 °C-2.5 times higher than the pristine QPPO membrane. This significant improvement in IC results from the synergistic effects of hydrophilic and hydrophobic microphase separation structures, which optimize ion transport for WE applications. Fig. 11d further compares the OH^- IC and SWR of QPPO-NH_4-Mx-3.0 with the data from previous composite AEM studies [8,13–15,31,74–79]. The QPPO-NH_4-Mx-3.0 membrane outperforms earlier results, achieving the highest IC alongside a balanced SWR. This balance highlights the successful optimization of membrane properties, representing a significant advancement in AEM in the present study for WE applications.

To further elucidate the structural organization induced by MXene incorporation, small-angle X-ray scattering (SAXS) analysis was performed in conjunction with AFM imaging. The pristine QPPO membrane exhibited only a broad scattering halo, corresponding to a characteristic d-spacing of approximately 1.78 nm (Fig. 12), indicative of a largely homogeneous morphology with limited ionic clustering. In contrast, the MXene-containing membranes displayed distinct additional scattering peaks at d-spacings of 2.06–4.27 nm, which became more prominent with increasing MXene content. These features signify the emergence of periodic nanodomains, reflecting enhanced microphase separation between hydrophilic and hydrophobic regions within the polymer matrix.

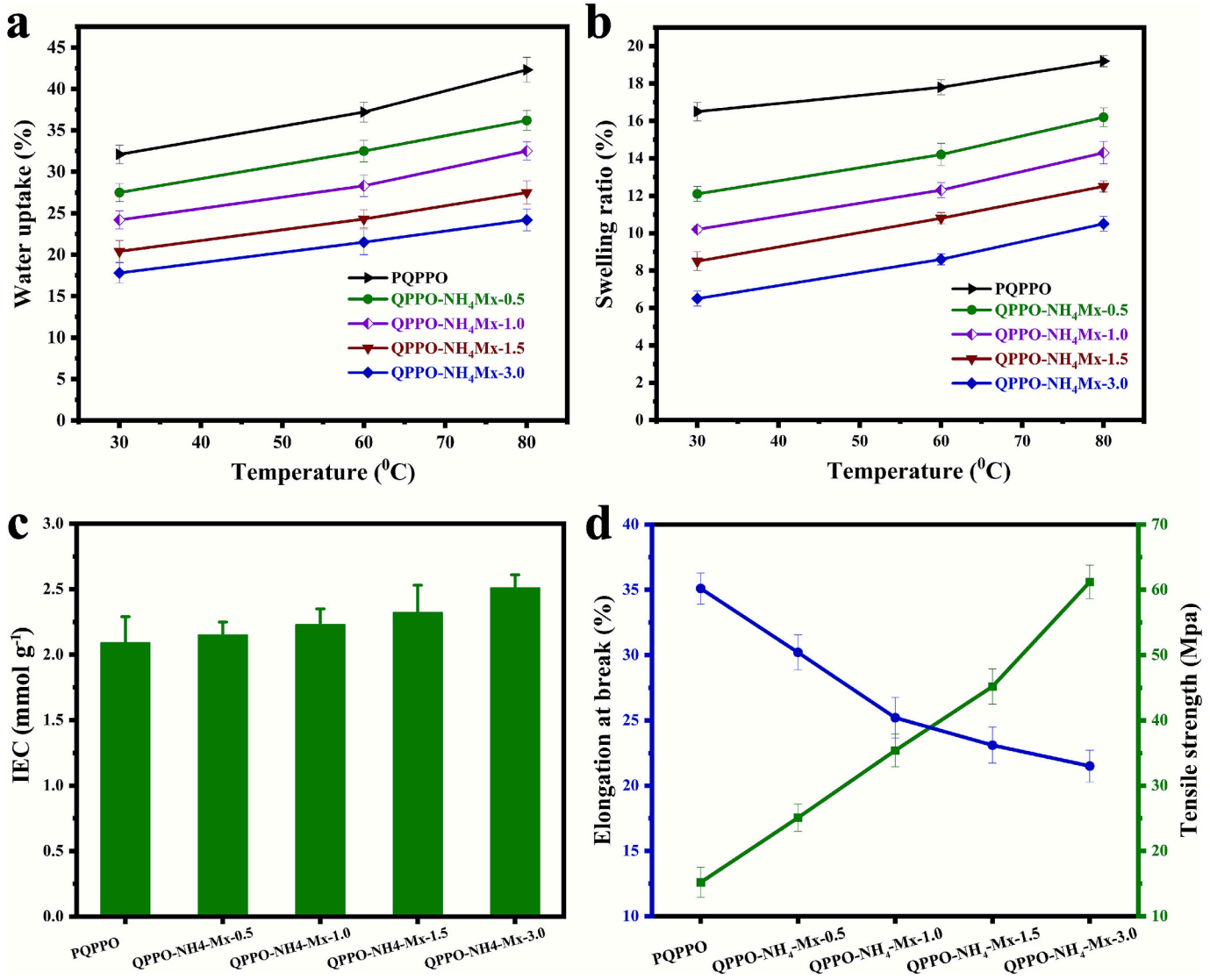

Fig. 10. Dimensional and mechanical properties of AEMs; (a) Water uptake (%), (b) swelling ratio (%), c) ion exchange capacity (mmol g^{-1}) and d) mechanical strength (tensile strength and elongation at break).

Complementary AFM phase images further confirmed this behavior, showing well-defined bright and dark contrast regions in the MXene-modified membranes, corresponding to ionic (hydrophilic) and non-ionic (hydrophobic) domains, respectively. Such morphological evolution strongly supports the formation of continuous, interconnected ion-transport pathways facilitated by the two-dimensional MXene sheets, which serve as physical templates promoting nanoscale segregation and interfacial ion clustering. Together, the SAXS and AFM analyses provide direct experimental evidence of microphase-separated architecture in the nanocomposite membranes, validating the proposed mechanism of enhanced OH^- IC through the development of ordered hydrophilic domains.

3.3.4. Alkaline and thermal stability of the composite AEMs

The alkaline stability study provides critical insights into the performance stability and service life of AEMs under harsh alkaline electrolytic conditions [31,80]. The residual OH^- IC over time, as shown in Fig. 13a, highlights the enhanced performance of nanocomposite AEMs compared to the pristine QPPO membrane. The PQPPO membrane shows a steep decline in remaining IC, maintaining only 33.2 % after 3 weeks, demonstrating poor alkaline stability. In contrast, the inclusion of NH_4^+-$Ti_2C_3T_x$ significantly improves IC retention. Increasing MXene content enhances alkaline stability, with QPPO-NH_4-Mx-3.0 retaining 80.2 % of its initial IC after 21 days.The QPPO-NH_4-Mx-1.0 and QPPO-NH_4-Mx-1.5 AEMs also show substantial improvements (73.4 and 76.3 % residual IC, respectively) compared to the pristine membrane.

This enhancement arises from MXene's inherent chemical stability under high-pH conditions and its ability to mitigate polymer degradation, including acting as radical scavengers that reduce oxidative degradation [81]. These interactions improve the compatibility and dispersion of MXene within the membrane, enhancing the stability and reducing the likelihood of chemical attack by OH^- ions [81]. Moreover, the improved alkaline stability of the nanocomposite membranes can be attributed to both physical and chemical stabilization effects imparted by MXene. The two-dimensional NH_4^+-$Ti_3C_2T_x$ sheets act as barriers against OH^- ion diffusion, effectively protecting the quaternary ammonium sites of QPPO from nucleophilic degradation. Furthermore, the strong interfacial interactions between MXene surface terminations (-O, -OH, -F, -NH_2) and the QPPO backbone enhance structural rigidity and suppress chain motion, thereby retarding degradation. Additionally, the MXene nanosheets themselves are relatively stable under alkaline conditions, and their encapsulation within the polymer matrix further minimizes any potential surface oxidation or leaching during the stability test. These combined effects explain the improved chemical

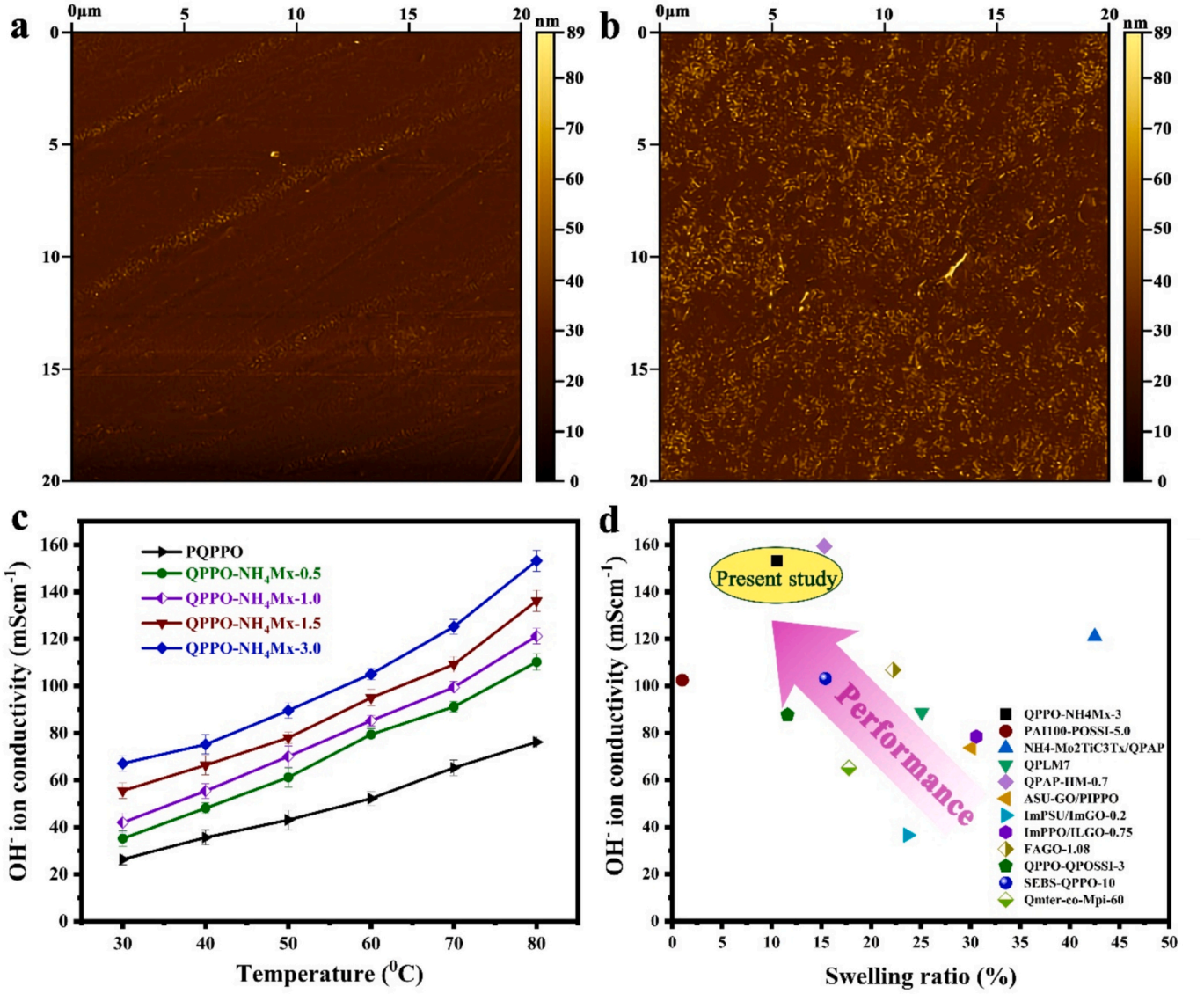

Fig. 11. AFM phase-contrast micrographs of (a) pristine QPPO membrane, (b) QPPO-NH_4-Mx-3.0 AEM, (c) OH^- ion conductivity of nanocomposite AEMs at varying temperatures and (d) comparison of OH^- ion conductivity vs swelling ratio of the nanocomposite AEMs in this study with previous studies reported in the state-of-the-art literature.

durability of the nanocomposite membranes in alkaline media. Among the nanocomposite AEMs, QPPO-NH_4-Mx-3.0 exhibited the best performance, retaining 80.2 % of its IC after 21 days. Notably, QPPO-NH_4-Mx-1.0 and QPPO-NH_4-Mx-1.5 AEMs also substantially improved by retaining 73.4 and 76.3 % residual IC, respectively, compared to the pristine QPPO membrane, but QPPO-NH_4-Mx-3.0 membrane stands out as the most promising candidate for long-term alkaline water electrolysis due to its superior IC retention capacity in alkaline environments.

After confirming alkaline stability, we also explored the changes in the membrane's thermal stability. The operational temperature of AEMWE typically ranges between 30 and 80 °C to ensure optimal IC and electrode kinetics. However, the thermal stability of AEMs at higher temperatures is crucial for evaluating their durability and performance under extreme conditions. To this end, we assessed the thermal stability of composite AEMs up to 700 °C. The TGA results are presented in Fig. 13b, representing the weight loss of AEMs against temperatures. The findings revealed distinct thermal behaviors across different temperature regions, providing insights into the influence of NH_4^+-functionalized MXene on the degradation patterns and residual weight of the AEMs. All the AEMs showed decomposition in four distinct stages.

Below 200 °C, the membranes exhibit very negligible weight loss, retaining ~100 % initial weight. This indicated comparable thermal stability in the absence of significant moisture or volatile component release. However, between 200 and 400 °C, weight loss becomes more pronounced, with the virgin QPPO membrane retaining significant weight than its composite counterparts. This feature indicated that the NH_4^+ group of the functionalized Mxene could decompose earlier, likely due to the degradation or weakly bound organic components at that temperature [82]. Between 400 and 600 °C, all the AEMs experienced significant weight loss, reflecting the breakdown of the core polymer backbone. Interestingly, the composite membranes outperform the pristine QPPO membrane in this range, with higher MXene content contributing to improved thermal stability. This trend is attributed to the reinforcement effects of MXene, which delayed the degradation of the QPPO matrix by providing structural stability and enhancing thermal resistance [83].

Residual weights beyond 600 °C show notable differences among the AEMs. The QPPO-NH_4-Mx-0.5 retains the highest residual weight (35.95 %), followed by pristine QPPO (34.64 %), QPPO-NH_4-Mx-3.0 (34.19 %), QPPO-NH_4-Mx-1.5 (33 %), and QPPO-NH_4-Mx-1.0 (31.23

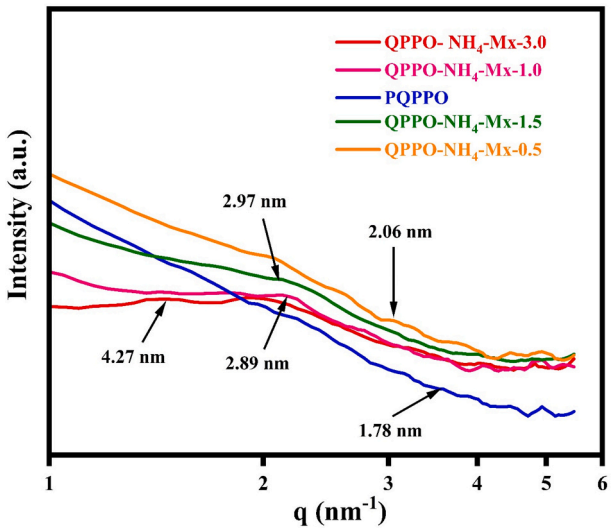

Fig. 12. Small-angle X-ray scattering (SAXS) profile of the nanocomposite AEMs. QPPO-NH_4-Mx-3.0 AEM showed a d-spacing of 4.27 nm corresponding to periodic nanodomains, reflecting enhanced microphase separation between hydrophilic and hydrophobic regions within the polymer matrix, which further supports the AFM results.

%). Overall, the differences in residual weight (%) loss among the composite AEMs were negligible, falling within a 4.75 % range, and can be considered insignificant for practical applications. It is noteworthy that, while alkaline IC retention increases with MXene content, the residual thermal weights do not follow a simple monotonic trend. This is due to the combined effects of early NH_4^+ decomposition, variations in polymer backbone stability, and complex polymer-MXene interactions influencing the thermal degradation behavior. These results suggested that the incorporation of NH_4^+-$Ti_3C_2T_x$ effectively enhances the thermal stability of composite AEMs, particularly at elevated temperatures.

3.3.5. *Cell performances and lab-scale durability analysis*

In this study, based on the dimensional, electrochemical, mechanical, alkaline and thermal stability analysis, QPPO-NH_4-Mx-3.0 AEM was identified as the best-performing membrane for AEMWE. Thus, cell performance and durability studies were executed with this membrane. The test was conducted at a constant temperature of 60 °C under two different alkaline environments, 1 M and 0.1 M KOH, to assess its efficiency and suitability for real-world applications. The results, presented in Fig. 14a, highlight the excellent electrochemical performance of the membrane. The current density increases steadily with voltage under both alkaline electrolytes, but the performance was consistently superior in 1 M KOH. The highest current densities were recorded at 2.1 and 1.68 A cm^{-2} for 1 M and 0.1 M KOH electrolytes, respectively. The cell performance demonstrated that current density increased by 25 % for 1 M KOH compared to 0.1 M KOH. This trend is observed across all voltage levels, demonstrating the critical role of electrolyte concentrations in enhancing cell performance. The higher ionic conduction in 1 M KOH reduces resistance and facilitates more efficient OH^- ion transport through the membrane, significantly boosting its efficiency and current density [84,85]. The improved performance of QPPO-NH_4-Mx-3.0 in a higher alkaline environment could be attributed to its unique structural properties. The incorporation of NH_4^+-$Ti_2C_3T_x$ MXene developed robust microphase structures that provide well-defined ionic channels, optimizing hydroxyl ion transport [86–88]. Additionally, the membrane's high structural stability minimizes ionic resistance, allowing it to perform consistently. The lab-scale durability analysis was performed at two specific current densities of 0.5 and 1.0 A cm^{-2} to cross-check the voltage decay rate over time up to 150 h (Figs. 14b-c). The results demonstrated excellent and robust performance of the cell with minimal voltage decay at both applied current densities. At an industrially relevant current density of 1.0 A cm^{-2}, the cell maintained stable operation with a voltage decay rate of 1.5 mVh^{-1}. At 0.5 A cm^{-2}, the voltage decay rate was even lower at 0.5 mVh^{-1}.

These findings confirm that QPPO-NH_4-Mx-3.0 not only excels in alkaline stability but also delivers outstanding cell performance and robust and sustained durability of the cell up to 150 h of electrolysis, making it an excellent candidate for advanced AEMWE. Since the voltage decay rate during continuous electrolysis was negligible, this indicates excellent long-term stability of the QPPO-NH_4-Mx-3.0's AEM. This minimal decline suggests that the performance loss primarily arises from minor interfacial resistance increases or surface oxidation of the catalyst, rather than from intrinsic degradation of the membrane itself. The stable IC and chemical integrity of the nanocomposite membrane after the test further confirm its superior alkaline stability. Although electrochemical impedance spectroscopy (EIS) data were not collected in this study, future work will employ pre- and post-durability EIS analysis to quantitatively differentiate resistance contributions from the

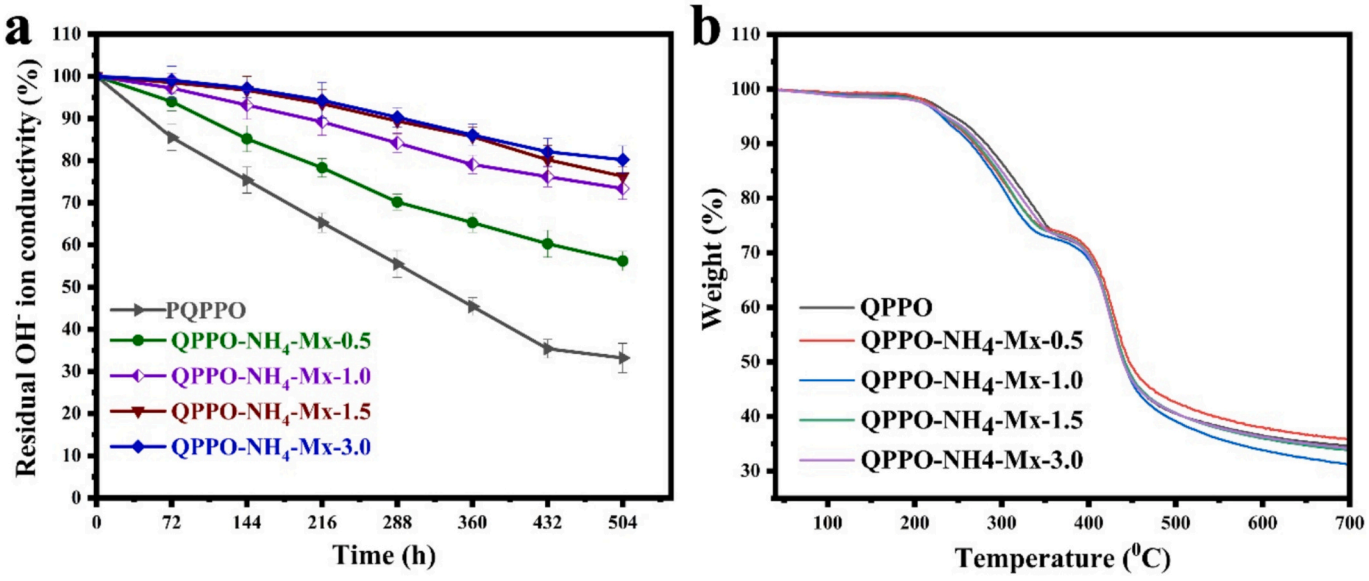

Fig. 13. (a) Alkaline stability of the composite AEMs and (b) thermal stability of the composite AEMs.

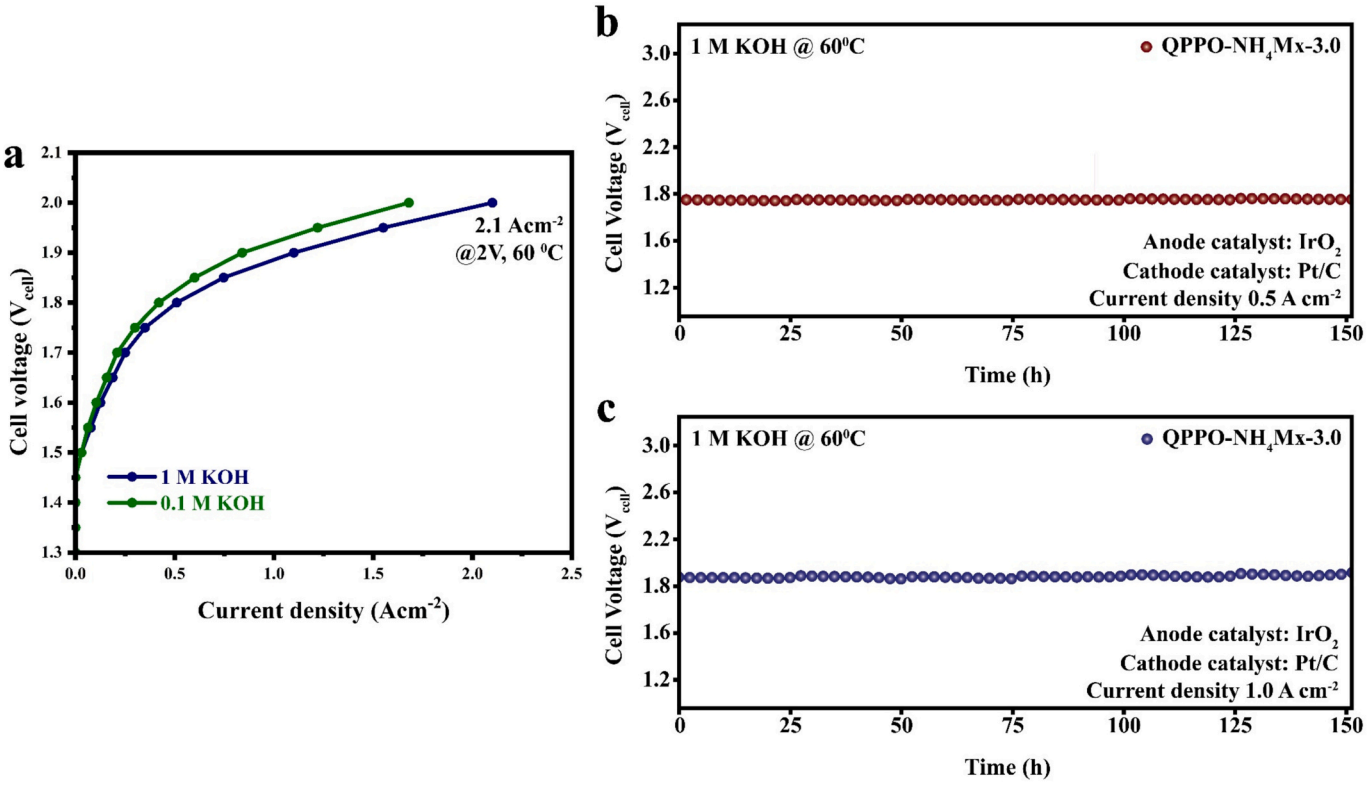

Fig. 14. (a) Cell performances (I-V curve) of QPPO-NH_4-Mx-3.0, (b) durability analysis at 0.5 A cm^{-2} and (c) durability analysis at 1.0 A cm^{-2}.

membrane, electrode, and interfacial regions.

3.3.6. *Working mechanisms of nanocomposite AEMs*

According to our hypothesis, the core working mechanism of the composite AEMs in this study is the formation of a hydrophilic-hydrophobic MIPS structure between the QPPO polymer matrix and MXene nanofillers (Fig. 15), supported by AFM and SAXS analysis. This MIPS structure is essential in overcoming the trade-offs between dimensional stability, mechanical strength, and electrochemical performance typically observed in AEMs. By promoting the controlled organization of hydrophilic and hydrophobic domains, the incorporation of MXene improves key properties, which ultimately improves the overall cell performance in AEMWE [15]. The QPPO polymer backbone, which is hydrophobic, provides structural strength and dimensional stability to the membrane, while the hydrophilic MXene nanofillers interact with the polymer to form well-defined ionic domains. These domains absorb water, facilitating efficient OH^- ion transport, while simultaneously restricting excessive swelling by maintaining a balance between the hydrophilic and hydrophobic phases. This phase separation not only enhances IC but also prevents uncontrolled water uptake, leading to long-term membrane stability [31]. The MXene nanofillers reinforce the PPO matrix, preventing swelling and mechanical degradation, thus ensuring the membrane maintains its structural integrity even under hydration conditions. The hydrophobic QPPO backbone resists swelling, while the hydrophilic ionic domains absorb water to maintain ion transport, ensuring the membrane's dimensional stability and operational longevity [14].

The MIPS structure created by MXene incorporation also plays a crucial role in improving the electrochemical performance of the composite AEM. The phase-separated domains form a network of well-connected ion-conducting channels that reduce resistance and enhance OH^- IC. This leads to higher IC compared to conventional AEMs, which directly impacts the energy efficiency of AEMWE [97]. Recent studies have shown that AEMs with MIPS structures exhibit significantly higher current densities during WE than non-phase-separated membranes due to the larger effective surface area for ion conduction and optimized water retention [98]. Additionally, MXene's incorporation stabilizes the polymer matrix against hydroxide attack, improving the membrane's chemical and electrochemical durability in the highly alkaline environment of AEMWE. The enhanced MIPS structure reduces membrane resistance, leading to higher current densities and lower energy consumption during electrolysis. As a result, the MXene-reinforced PPO-based AEMs offer a balance of mechanical strength, dimensional stability, and enhanced IC, making them highly promising for efficient and durable hydrogen production through AEMWE [99].

3.3.7. *Comparative evaluation with commercial and other PPO-based AEMs reported in the state-of-the-art literature*

To contextualize the performance of the QPPO-NH_4-Mx-3.0 membrane, a comparative study was carried out against both commercially available AEMs (Table 2) and reported PPO-based AEMs (Table 3) in the literature. As shown in Table 2, the QPPO-NH_4-Mx-3.0 membrane exhibits a cell current density of 2.1 A cm^{-2} at 2.0 V and 60 °C in 1 M KOH, comparable to or better than several state-of-the-art commercial membranes such as Fumasep® FAA-3-50 (1.2 A cm^{-2} at 2.0 V) and Aemion™ AF1-HNN8–50 (1.8 A cm^{-2} at 2.0 V). The PiperION® self-supporting membrane (80 μm) achieves 2.3 A cm^{-2} under similar conditions but typically exhibits a higher voltage decay rate. Interestingly, QPPO-NH_4-Mx-3.0 maintains excellent durability, with a voltage decay rate of only 1.5 mV h^{-1} over 150 h, outperforming many commercial AEMs that experience decay rates between 5 and 50 mV h^{-1}. This demonstrates that although its initial current density is moderate, the operational stability and interfacial robustness of QPPO-NH_4-Mx-3.0 have significant competitive advantages. The outstanding durability is attributed to the MXene-reinforced QPPO matrix, which minimizes swelling, maintains dimensional stability, and suppresses OH^--induced degradation.

Table 3 summarizes previously reported PPO-based membranes, enabling a direct performance-to-structure comparison. The present

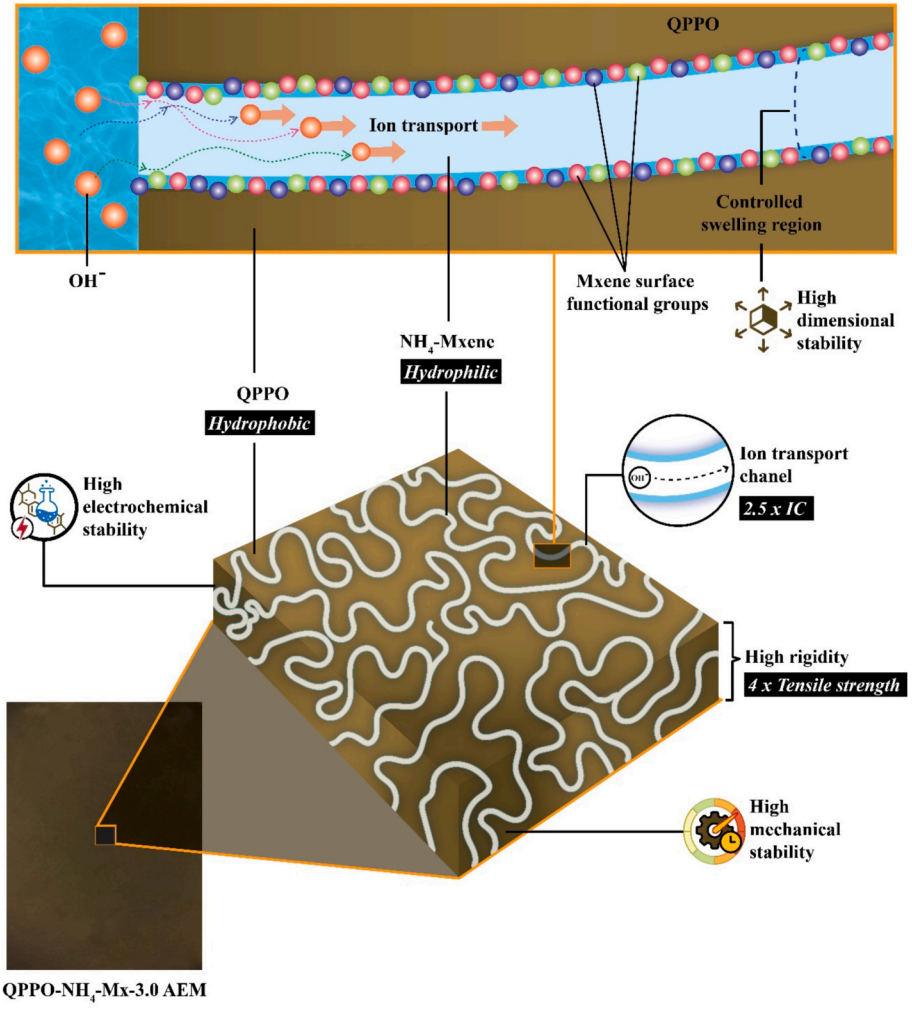

Fig. 15. The working mechanisms of nanocomposite AEM in the present study for sustainable WE performance.

Table 2
Comparison of cell performances of the commercially available AEMs with the present study.

AEMs		Temperature (°C)	Electrolytes	Anode	Cathode	Cell performance @2 V (A cm^{-2})	Durability			References
							Applied current (A cm^{-2})	Voltage decay rate (mVh^{-1})	Duration (h)	
Fumasep®	FAA-3-50	60	1 M KOH	IrO_2	Pt/C	1.20	1.0	1.0	120	[8]
	FAA-3-50	60	1 M KOH	$NiFe_2O_4$	Pt/C	2.74	–	5.0	70	[15]
Sustainion® X37–50	Grade RT	60	1 M KOH	Stainless steel	Pt/C	2.74	1.0	1.56	205	[14]
	Grade T	60	1 M KOH	IrO_2	Pt/C	1.80	–	–	–	[31]
Aemion™	AF1-HNN8–50	60	1 M KOH	NiS_2/Ni_3S_4	Pt/C	1.8	0.5	0.12	500	[74]
	AF1-HNN8–50	60	1 M KOH	Ni/NiO	Pt/C	1.06	1.0	1.7	50	[75]
Tokuyama	A201	60	1 wt% K_2CO_3	Acta 3030® ($CuCoO_x$)	Acta 4030® (Ni/ (CeO_2 La_2O_3)/C)	1.0	0.5	0.5	200	[76]
	A201	60	1 M KOH	$NiFe_2O_4$	NiFeCo	2.0	–	–	–	[77]
PiperION®	Self-Supporting, 80 μm	80	1 M KOH	Stainless Steel	Pt/C	2.3	2.0	5.0	640	[78]
	Self-Supporting, 20 μm	60	1 M KOH	IrO_2	PtRu/C	5.5	0.5	0.29	309	[13]
Orion TM1		70	1 M KOH	IrO_2	Pt/C	2.75	0.5	55	50	[79]
QPPO-NH_4-Mx-3.0		60	1 M KOH	IrO_2	Pt/C	1.68	1.0	1.5	150	This study
QPPO-NH_4-Mx-3.0		60	0.1 M KOH	IrO_2	Pt/C	2.10	0.5	0.5	150	This study

Table 3
Comparative study of the dimensional, mechanical and electrochemical performances of PPO-based AEMs with the present study.

AEMs	Dimensional stability			Mechanical stability		OH^- IC (mS cm^{-1} at 80 °C)	Alkaline stability (Residual IC (%))	Single-cell performance (A cm^{-2} at 2.0 V)	Long-term durability		References
	WU (%	SWR (%)	IEC (mmol g^{-1})	TS (MPa)	EB (%)				Duration (h)	Voltage decay rate (mV h^{-1}) for 1 A cm^{-2}	
x-TriPPO-50SEBS	76.3	36.7	1.17	29.0	106.2	77.35	–	0.71	–	–	[89]
x-PPO-50SEBS	64.9	32.4	1.25	20.6	63.1	66.05	20	0.42	–	–	[89]
QPPO/PTFE	40	–	–	31	87	30	–	–	–	–	[90]
QPQT-30	77.7	18.1	0.83	13.7	4.8	42.0	–	0.87	–	–	[91]
C-QPAP-2-QPPO	15.7	3.4	2.19	50.7	105.1	139.4	86	1.44	30	–	[92]
QPPO-14	430	49	2.20	14	3.1	133.3	94	0.814	–	–	[93]
x-allyl-0.05-PPO	13.42	4.55	2.15	68.73	4.6	23.22	–	0.90	18	4.4	[94]
PBPA	140	44	2.60	35	55	123	–	4.0	3500	0.0065	[95]
20 % COFBrx-TPP	87.6	9.3	1.60	22	–	225.9	95.5	4.5	22	6.17	[96]
QPPO-NH_4-Mx-3.0	24.2	10.5	2.51	61.2	21.5	153.2	80.2	2.1	150	1.5	Present study

QPPO-NH_4-Mx-3.0 system exhibits one of the highest OH^- IC (153.2 mS cm^{-1} at 80 °C) among PPO derivatives, while maintaining low WU (24.2 %), SWR (10.5 %), and high tensile strength (61.2 MPa). This balance contrasts with other PPO-based AEMs, which often require higher hydration levels to reach comparable conductivities but at the expense of dimensional stability. In terms of AEMWE performance, QPPO-NH_4-Mx-3.0 achieves 2.1 A cm^{-2} at 2.0 V, which is among the best reported for PPO-based systems, while also providing superior long-term stability and simpler fabrication. The integration of MXene introduces a two-dimensional barrier and ionic-pathway reinforcement, by MIPS structure, offering improved mechanical and electrochemical stability without complex crosslinking chemistry. Overall, these results confirm that QPPO-NH_4-Mx-3.0 achieves a synergistic balance of high IC, mechanical strength, and durability, making it highly competitive with both commercial and literature-reported PPO-based membranes for AEMWE.

4. Conclusion and outlook

In this study, we successfully reinforced functionalized MXene nano-filler into the quaternized poly (phenylene oxide) (QPPO) to fabricate a series of nanocomposite anion exchange membranes (AEMs), focusing on the elimination of the trade-offs among various crucial performance parameters to ensure sustainable green hydrogen production. The nanocomposite AEMs showed controlled water uptake, swelling ratio and ion exchange capacity with incorporated MXene compared to the virgin QPPO membrane. The tensile strength (TS) of the AEMs ranged from 15.2 to 61.2 MPa, with the maximum TS recorded for QPPO-NH_4-Mx-3.0 at 61.2 MPa. The QPPO-NH_4-Mx-3.0 exhibited the best performance, achieving an impressive hydroxide (OH^-) ion conductivity (IC) of 153.2 mS cm^{-1} at 80 °C-2.5 times higher than that of the pristine QPPO membrane. The TGA results suggested that the incorporation of NH_4^+-$Ti_3C_2T_x$ effectively enhances the thermal stability of composite AEMs, particularly at elevated temperatures. We hypothesized that the core mechanism involved in the enhanced/controlled performance of composite AEMs in terms of dimensional, electrochemical, and mechanical stability is the hydrophobic-hydrophilic microphase separation structures (MIPS) within the AEMs, which were developed by the incorporation of NH_4^+-$Ti_3C_2T_x$. The maximum current densities were recorded at 2.1 and 1.68 A cm^{-2} for 1 M and 0.1 M KOH electrolytes, respectively, at 2 V for QPPO-NH_4-Mx-3.0, which is comparable to the recently developed AEMs available in the state-of-the-art literature and some of the commercial membranes. Furthermore, it showed excellent alkaline stability, retaining 80.2 % of its initial IC after three weeks of immersion in 1 M KOH at 60 °C. The lab-scale durability analysis was performed at two specific current densities of 0.5 and 1.0 A cm^{-2} to cross-check the voltage decay rate over time up to 150 h of electrolysis. The results demonstrated stable and robust performance of the cell with a minimal voltage decay of 0.5 and 1.5 mVh^{-1} for 0.5 and 1.0 A cm^{-2}, respectively. In essence, the QPPO-NH_4-Mx-3.0 could be one of the novel AEM materials for the advanced AEMWE. This membrane demonstrates substantial promise as a high-performance AEM for advancing AEMWE technology, paving the way for more efficient and reliable water electrolysis systems. As a proof-of-concept study, we identified a few specific limitations that need to be addressed in future to scale up this AEM commercially at an industrial scale AEMWE, as follows:

- The scaling up of AEM fabrication toward commercial application, with particular emphasis on further optimization and fine-tuning of AEM processing conditions.
- The dispersion of MXene nano-filler could be enhanced by surface engineering and adding highly dispersible and conductive materials, such as ionic liquids.
- Alkaline stability needs to be improved to some extent, and the duration of the alkaline stability test also needs to be increased. In this case, the blending of highly rigid ether-free polymer backbones such as poly(carbazole) and poly(biphenyl) could be the best option. These polymer backbones might also increase the IC and overall cell performance.
- To increase the mechanical strength, especially elongation at break, some ether-free flexible crosslinkers can be used, such as bis[2-(*N*,*N*-dimethylamino)ethyl] ether (BDME) and styrene-ethylene-butylene-styrene (SEBS).
- While the present membranes were evaluated for short-term durability, extended stability studies are essential. Accordingly, long-term cell tests of at least 1000 h will be prioritized to better replicate real-world operating conditions and validate the integration of AEMs into practical AEMWE electrolyzer systems.

CRediT authorship contribution statement

Mohammad Mahbub Kabir: Writing – original draft, Methodology, Formal analysis, Data curation, Conceptualization. **M.A. Zaed:** Writing – review & editing, Methodology. **Yeshi Choden:** Writing – review & editing, Investigation, Formal analysis, Data curation. **R. Saidur:** Writing – review & editing. **Leonard Tijing:** Writing – review & editing, Validation, Supervision, Data curation. **Sherub Phuntsho:** Writing – review & editing, Resources, Project administration, Formal analysis, Data curation. **Sang Yong Nam:** Writing – review & editing, Resources, Formal analysis. **Ho Kyong Shon:** Writing – review & editing, Validation, Supervision, Resources, Project administration, Investigation, Funding acquisition, Formal analysis, Conceptualization.

Declaration of competing interest

The authors declare no conflict of interest. Ho Kyong Shon serves as a co-Editor-in-Chief in Desalination journal, whereas the editorial and peer-review processes of this manuscript were administered by another Editor.

Acknowledgements

The Australian Research Council (ARC) industrial transformation research hub on nutrients in a circular economy (NiCE) (IH210100001) supported this research. This research was supported by Basic Science Research Program through the National Research Foundation of Korea (NRF) funded by the Ministry of Education (RS-2020-NR049575 and RS-2025-25397043). Mohammad Mahbub Kabir acknowledged the University of Technology Sydney President (UTSP) scholarship, International Research Scholarship from the University of Technology Sydney (UTS).

Data availability

Data will be made available on request.

References

[1] M.M. Kabir, K.S. Im, L. Tijing, Y. Choden, S. Phuntsho, M.F.K. Mamun, G. M. Sabur, S.Y. Nam, H.K. Shon, Integrated membrane distillation-solid electrolyte-based alkaline water electrolysis for enhancing green hydrogen production, Desalination 601 (2025) 118580, https://doi.org/10.1016/J.DESAL.2025.118580.

[2] M.M. Kabir, G.M. Sabur, M.F.K. Mamun, L. Arman, Y. Tijing, S. Choden, H.K. Shon Phuntsho, Hydrogels in next-generation energy solutions, Desalination 603 (2025) 118639, https://doi.org/10.1016/J.DESAL.2025.118639.

[3] G. Sriram, K. Dhanabalan, K.V. Ajeya, K. Aruchamy, Y.C. Ching, T.H. Oh, H. Y. Jung, M. Kurkuri, Recent progress in anion exchange membranes (AEMs) in water electrolysis: synthesis, physio-chemical analysis, properties, and applications, J. Mater. Chem. A Mater. 11 (2023) 20886–21008, https://doi.org/10.1039/d3ta04298g.

[4] G. Merle, M. Wessling, K. Nijmeijer, Anion exchange membranes for alkaline fuel cells: a review, J. Membr. Sci. 377 (2011) 1–35, https://doi.org/10.1016/j.memsci.2011.04.043.

[5] M.M. Kabir, G.M. Sabur, M.M. Akter, S.Y. Nam, K.S. Im, L. Tijing, H.K. Shon, Electrodialysis desalination, resource and energy recovery from water industries for a circular economy, Desalination 569 (2024), https://doi.org/10.1016/j.desal.2023.117041.

[6] D. Ion-Ebrasu, B.G. Pollet, S. Caprarescu, A. Chitu, R. Trusca, V. Niculescu, R. Gabor, E. Carcadea, M. Varlam, B.S. Vasile, Graphene inclusion effect on anion-exchange membranes properties for alkaline water electrolyzers, Int. J. Hydrogen Energy 45 (2020) 17057–17066, https://doi.org/10.1016/j.ijhydene.2020.04.195.

[7] R. Yang, P. Dai, S. Zhang, R.W. Xu, S. Hong, W.F. Lin, Y.X. Wu, In-situ synthesis of cross-linked imidazolium functionalized poly(styrene-b-isobutylene-b-styrene) for anion exchange membranes, Polymer (Guildf) 224 (2021), https://doi.org/10.1016/j.polymer.2021.123682.

[8] V.D.C. Tinh, V.D. Thuc, Y. Jeon, G.Y. Gu, D. Kim, Highly durable poly(arylene piperidinium) composite membranes modified with polyhedral oligomeric silsesquioxane for fuel cell and water electrolysis application, J. Membr. Sci. 660 (2022) 120903, https://doi.org/10.1016/J.MEMSCI.2022.120903.

[9] M. Naguib, M. Kurtoglu, V. Presser, J. Lu, J. Niu, M. Heon, L. Hultman, Y. Gogotsi, M.W. Barsoum, Two-dimensional nanocrystals produced by exfoliation of Ti3ALC2, in: MXenes: From Discovery to Applications of Two-Dimensional Metal Carbides and Nitrides, 2023, pp. 15–29, https://doi.org/10.1201/9781003306511-4/TWO-DIMENSIONAL-NANOCRYSTALS-PRODUCED-EXFOLIATION-TI3ALC2-MICHAEL-NAGUIB-MURAT-KURTOGLU-VOLKER-PRESSER-JUN-LU-JUNJIE-NIU-MIN-HEON-LARS-HULTMAN-YURY-GOGOTSI-MICHEL-BARSOUM.

[10] M.M. Kabir, M.M. Akter, Z. Huang, L. Tijing, H.K. Shon, Hydrogen production from water industries for a circular economy, Desalination 554 (2023), https://doi.org/10.1016/j.desal.2023.116448.

[11] K. Im, M. Park, M.M. Kabir, W. Sohn, Y. Choo, H.K. Shon, S.Y. Nam, Human urine electrolysis for simultaneous green hydrogen and liquid fertilizer production for a circular economy: a proof of concept, Desalination 570 (2024), https://doi.org/10.1016/j.desal.2023.117059.

[12] S. Yu, P. Zhou, J. Hao, Y. Zhou, Research progress of functionalized graphite oxide based alkaline anion exchange membrane for fuel cells, Polymer (Guildf) 283 (2023), https://doi.org/10.1016/j.polymer.2023.126256.

[13] J. Han, C. Liu, C. Deng, Y. Zhang, W. Song, X. Zheng, X. Liu, Y. Zhang, X. Yang, Z. Ren, M. Hu, L. Xiao, L. Zhuang, Mechanically robust and highly conductive semi-interpenetrating network anion exchange membranes for fuel cell applications, J. Power Sources 548 (2022) 232097, https://doi.org/10.1016/J.JPOWSOUR.2022.232097.

[14] Z. Yang, M. Zhang, Z. Zhao, W. Lan, X. Zhang, M. Fan, Application of 2D nanomaterial MXene in anion exchange membranes for alkaline fuel cells: improving ionic conductivity and power density, Int. J. Hydrogen Energy 47 (2022) 18122–18138, https://doi.org/10.1016/j.ijhydene.2022.03.269.

[15] J. Zhang, Q. Ling, Q. Wang, C. Xu, H. Wei, R. Espiritu, A quaternized poly(aryl piperidinium)/ quaternary MXene based three-layer membrane for alkaline anion exchange membrane fuel cells, Int. J. Hydrogen Energy 56 (2024) 1–6, https://doi.org/10.1016/J.IJHYDENE.2023.11.299.

[16] I. Arunkumar, A.R. Kim, S.H. Lee, D.J. Yoo, Enhanced fumion nanocomposite membranes embedded with graphene oxide as a promising anion exchange membrane for fuel cell application, Int. J. Hydrogen Energy 52 (2024) 139–153, https://doi.org/10.1016/j.ijhydene.2022.10.184.

[17] Q. Yang, C.X. Lin, F.H. Liu, L. Li, Q.G. Zhang, A.M. Zhu, Q.L. Liu, Poly (2,6-dimethyl-1,4-phenylene oxide)/ionic liquid functionalized graphene oxide anion exchange membranes for fuel cells, J. Membr. Sci. 552 (2018) 367–376, https://doi.org/10.1016/j.memsci.2018.02.036.

[18] V. Vijayakumar, T.Y. Son, H.J. Kim, S.Y. Nam, A facile approach to fabricate poly (2,6-dimethyl-1,4-phenylene oxide) based anion exchange membranes with extended alkaline stability and ion conductivity for fuel cell applications, J. Membr. Sci. 591 (2019), https://doi.org/10.1016/j.memsci.2019.117314.

[19] V. Vijayakumar, T.Y. Son, K.S. Im, J.E. Chae, H.J. Kim, T.H. Kim, S.Y. Nam, Anion exchange composite membranes composed of quaternary ammonium-functionalized poly(2,6-dimethyl-1,4-phenylene oxide) and silica for fuel cell application, ACS Omega 6 (2021) 10168–10179, https://doi.org/10.1021/ACSOMEGA.1C00247.

[20] G. Das, B.J. Park, J. Kim, D. Kang, H.H. Yoon, Quaternized cellulose and graphene oxide crosslinked polyphenylene oxide based anion exchange membrane, Sci. Rep. 9 (2019) 1–11, doi:10.1038/S41598-019-45947-W; TECHMETA=128,131,140;SUBJMETA=1028,301,455,638,639,923,957; KWRD=NANOCOMPOSITES,POLYMERS.

[21] N. Chen, C. Long, Y. Li, D. Wang, H. Zhu, High-performance layered double hydroxide/poly(2,6-dimethyl-1,4-phenylene oxide) membrane with porous sandwich structure for anion exchange membrane fuel cell applications, J. Membr. Sci. 552 (2018) 51–60, https://doi.org/10.1016/j.memsci.2018.01.045.

[22] T.T. Letsau, P.P. Govender, P.F. Msomi, Imidazolium-quaternized poly(2,6-dimethyl-1,4-phenylene oxide)/zeolitic imidazole framework-8 composite membrane as polymer electrolyte for fuel-cell application, Polymers 14 (2022) 595, https://doi.org/10.3390/POLYM14030595.

[23] K. Li, J. Chen, M. Guan, S. Tang, Novel multi-channel anion exchange membrane based on poly ionic liquid-impregnated cationic metal-organic frameworks, Int. J. Hydrogen Energy 45 (2020) 17813–17823, https://doi.org/10.1016/J.IJHYDENE.2020.04.196.

[24] J. Chen, M. Guan, K. Li, S. Tang, Novel quaternary ammonium-functionalized covalent organic frameworks/poly(2,6-dimethyl-1,4-phenylene oxide) hybrid anion exchange membranes with enhanced Ion conductivity and stability, ACS Appl. Mater. Interfaces 12 (2020) 15138–15144, https://doi.org/10.1021/ACSAMI.9B22916/SUPPL_FILE/AM9B22916_SI_001.PDF.

[25] J. Chen, M. Guan, K. Li, S. Tang, High-performance COF-based composite anion exchange membrane sandwiched by GO layers for alkaline H2/O2 fuel cell application, J. Ind. Eng. Chem. 104 (2021) 136–145, https://doi.org/10.1016/J.JIEC.2021.08.016.

[26] W. Yang, J. Yan, S. Liu, J. Zhou, J. Liu, Q. Zhang, Y. Yan, Macromolecular crosslink of imidazole functionalized poly(vinyl alcohol) and brominated poly (phenylene oxide) for anion exchange membrane with enhanced alkaline stability and ionic conductivity, Int. J. Hydrogen Energy 46 (2021) 37007–37016, https://doi.org/10.1016/J.IJHYDENE.2021.08.184.

[27] F. Xu, K. Qiu, J. Li, B. Lin, J. Ding, Cross-linked anion exchange membranes with flexible, long-chain, bis-imidazolium cation cross-linker, Int. J. Hydrogen Energy 46 (2021) 37039–37048, https://doi.org/10.1016/J.IJHYDENE.2021.08.181.

[28] W.K. Ng, W.Y. Wong, K.S. Loh, M.S. Masdar, N. Shaari, M.M. Pang, A comprehensive overview of polyphenylene oxide-based anion exchange membranes from the perspective of ionic conductivity and alkaline stability, J. Ind. Eng. Chem. 138 (2024) 49–71, https://doi.org/10.1016/J.JIEC.2024.04.012.

[29] X. Zhang, Z. Yu, J. Tang, J. Huang, X. Tang, B. Lin, S. Xia, Mxenes as inorganic fillers for the construction of poly(aryl piperidinium) anion exchange membranes with microphase separation structures to enhance ionic conductivity, Fuel 365 (2024), https://doi.org/10.1016/j.fuel.2024.131177.
[30] V. Vijayakumar, T.Y. Son, H.J. Kim, S.Y. Nam, A facile approach to fabricate poly (2,6-dimethyl-1,4-phenylene oxide) based anion exchange membranes with extended alkaline stability and ion conductivity for fuel cell applications, J. Membr. Sci. 591 (2019), https://doi.org/10.1016/j.memsci.2019.117314.
[31] X. Zhang, Z. Yu, J. Tang, J. Huang, X. Tang, B. Lin, S. Xia, Mxenes as inorganic fillers for the construction of poly(aryl piperidinium) anion exchange membranes with microphase separation structures to enhance ionic conductivity, Fuel 365 (2024) 131177, https://doi.org/10.1016/J.FUEL.2024.131177.
[32] K. Im, M. Park, M.M. Kabir, W. Sohn, Y. Choo, H.K. Shon, S.Y. Nam, Human urine electrolysis for simultaneous green hydrogen and liquid fertilizer production for a circular economy: a proof of concept, Desalination 570 (2024), https://doi.org/10.1016/j.desal.2023.117059.
[33] V. Vijayakumar, T.Y. Son, H.J. Kim, S.Y. Nam, A facile approach to fabricate poly (2,6-dimethyl-1,4-phenylene oxide) based anion exchange membranes with extended alkaline stability and ion conductivity for fuel cell applications, J. Membr. Sci. 591 (2019) 117314, https://doi.org/10.1016/J.MEMSCI.2019.117314.
[34] M. Naguib, M. Kurtoglu, V. Presser, J. Lu, J. Niu, M. Heon, L. Hultman, Y. Gogotsi, M.W. Barsoum, Two-dimensional nanocrystals produced by exfoliation of Ti3AlC2, Adv. Mater. 23 (2011) 4248–4253, https://doi.org/10.1002/ADMA.201102306.
[35] A.W. Schuppe, T.R. Newhouse, Assembly of the limonoid architecture by a divergent approach: Total synthesis of (±)-andirolide N via (±)-8α-hydroxycarapin, J. Am. Chem. Soc. 139 (2017) 631–634, https://doi.org/10.1021/JACS.6B12268/SUPPL_FILE/JA6B12268_SI_003.CIF.
[36] S. Kumar, N. Kumari, Y. Seo, MXenes: versatile 2D materials with tailored surface chemistry and diverse applications, J. Energy Chem. 90 (2024) 253–293, https://doi.org/10.1016/J.JECHEM.2023.11.031.
[37] M. Alhabeb, K. Maleski, B. Anasori, P. Lelyukh, L. Clark, S. Sin, Y. Gogotsi, Guidelines for synthesis and processing of two-dimensional titanium carbide (Ti3C2Tx MXene), Chem. Mater. 29 (2017) 7633–7644, https://doi.org/10.1021/ACS.CHEMMATER.7B02847/SUPPL_FILE/CM7B02847_SI_002.MP4.
[38] Y. Gogotsi, B. Anasori, The rise of MXenes, ACS Nano 13 (2019) 8491–8494, https://doi.org/10.1021/ACSNANO.9B06394/ASSET/IMAGES/MEDIUM/NN9B06394_0005.GIF.
[39] Z. Cheng, Y. Cao, R. Wang, X. Liu, F. Fan, Y. Huang, Multifunctional MXene-based composite films with simultaneous terahertz/gigahertz wave shielding performance for future 6G communication, J. Mater. Chem. A Mater. 11 (2023) 5593–5605, https://doi.org/10.1039/D2TA09879B.
[40] V.R. Bhaviripudi, J. Pani, D.P. Pabba, D.F. Zambrano, R. Udayabhaskar, A. Rosenkranz, D. Moncada, R. Espinoza-González, H. Borkar, R. Aepuru, Augmented surface terminations on few-layer MXene (Ti3C2Tx) with superior electrochemical behavior for energy storage applications, J. Mater. Sci. Mater. Electron. 35 (2024) 1–11, https://doi.org/10.1007/S10854-024-12760-9/METRICS.
[41] A. Çelik, Y. Aksoy, Ö. Hanay, M. Yegin, Y. Köse, K. Demirelli, H. Hasar, Fabrication and characterization of Ti3C2TX MXene-based bipolar membrane, J. Appl. Electrochem. (2024) 1–14, https://doi.org/10.1007/S10800-024-02231-8/METRICS.
[42] M. Ghidiu, M. Naguib, M.W. Barsoum, Chemical and electrochemical intercalation of ions and molecules into MXenes, in: 2D Metal Carbides and Nitrides (MXenes): Structure, Properties and Applications, 2019, pp. 161–175, https://doi.org/10.1007/978-3-030-19026-2_10.
[43] J. Luo, Interlayer structural engineering of 2D MXene for electrochemical energy storage, advances in sustainable energy: policy, Mater. Dev. (2021) 451–478, https://doi.org/10.1007/978-3-030-74406-9_16.
[44] M.A. Zaed, K.H. Tan, R. Saidur, M. Rezakazemi, A.K. Pandey, Crafting 2D MXene composite from recycled materials for solar-driven desalination, Sep. Purif. Technol. 376 (2025) 134110, https://doi.org/10.1016/J.SEPPUR.2025.134110.
[45] M.A. Zaed, K.H. Tan, R. Saidur, A.K. Pandey, J. Cherusseri, Low-cost synthesis of Ti3C2Tx MXene-based sponge for solar steam generation and clean water production, Ceram. Int. 50 (2024) 27910–27922, https://doi.org/10.1016/J.CERAMINT.2024.05.086.
[46] A.G. Juandito, D.S. Khaerudini, S. Priyono, G.T.M. Kadja, D. Djuhana, M. Khalil, Ultrasonic-assisted dealumination enhances the performance of Ti3C2Tx MXene as an anode in Li-ion battery, J. Nanopart. Res. 26 (2024) 1–11, https://doi.org/10.1007/S11051-024-06022-2/METRICS.
[47] G. Shukla, V.K. Shahi, Well-designed mono- and di-functionalized comb-shaped poly(2,6-dimethylphenylene oxide) based alkaline stable anion exchange membrane for fuel cells, Int. J. Hydrogen Energy 43 (2018) 21742–21749, https://doi.org/10.1016/J.IJHYDENE.2018.04.027.
[48] G.A. Arı, C. Iojoiu, J. Sanchez, Synthesis and characterization of stable anion exchange membranes: the addition of electron-withdrawing group, Süleyman Demirel University J. Nat. Appl. Sci. 20 (2016) 442–447, https://doi.org/10.19113/SDUFBED.67145.
[49] M. Manohar, D. Kim, Enhancement of alkaline conductivity and chemical stability of quaternized poly(2,6-dimethyl-1,4-phenylene oxide) alkaline electrolyte membrane by mild temperature benzyl bromination, RSC Adv. 10 (2020) 36704–36712, https://doi.org/10.1039/d0ra06852g.
[50] K.H. Gopi, S.G. Peera, S.D. Bhat, P. Sridhar, S. Pitchumani, Preparation and characterization of quaternary ammonium functionalized poly(2,6-dimethyl-1,4-phenylene oxide) as anion exchange membrane for alkaline polymer electrolyte fuel cells, Int. J. Hydrogen Energy 39 (2014) 2659–2668, https://doi.org/10.1016/j.ijhydene.2013.12.009.
[51] X. Zhan, C. Si, J. Zhou, Z. Sun, MXene and MXene-based composites: synthesis, properties and environment-related applications, Nanoscale Horiz. 5 (2020) 235–258, https://doi.org/10.1039/C9NH00571D.
[52] M.R. Maurya, M.S. Sha, L. Latrous, A. Megriche, K.K. Sadasivuni, Engineering PLA-MXene nanocomposite with balanced mechanical properties for enhanced shape memory effect, J. Polym. Res. 31 (2024) 1–10, https://doi.org/10.1007/S10965-024-04193-Z/FIGURES/8.
[53] J. Zhang, H. Cheng, A. Abd-El-Aziz, X. Zhang, N. Ma, A.S. Abd-El-Aziz, Design of an efficient, low-cost and high photothermal conversion antibacterial membrane for seawater using a Ti3C2Tx MXene composite with polyethyleneimine and silver nanoparticles, J. Inorg. Organomet. Polym. Mater. (2025) 1–16, https://doi.org/10.1007/S10904-024-03552-Z/METRICS.
[54] M. Mozafari, M. Soroush, Surface functionalization of MXenes, Mater. Adv. 2 (2021) 7277–7307, https://doi.org/10.1039/D1MA00625H.
[55] J. Huang, Z. Yu, J. Tang, P. Wang, X. Zhang, J. Wang, X. Lei, A non-cationic crosslinking strategy to improve the performance of anion exchange membranes based on poly(aryl piperidinium) for fuel cells, Colloids Surf. A Physicochem. Eng. Asp. 674 (2023) 131890, https://doi.org/10.1016/J.COLSURFA.2023.131890.
[56] X. Gao, H. Yu, B. Qin, J. Jia, J. Hao, F. Xie, Z. Shao, Enhanced water transport in AEMs based on poly (styrene–ethylene–butylene–styrene) triblock copolymer for high fuel cell performance, Polym. Chem. 10 (2019) 1894–1903, https://doi.org/10.1039/C8PY01618F.
[57] M. Manohar, D. Kim, Enhancement of alkaline conductivity and chemical stability of quaternized poly(2,6-dimethyl-1,4-phenylene oxide) alkaline electrolyte membrane by mild temperature benzyl bromination, RSC Adv. 10 (2020) 36704–36712, https://doi.org/10.1039/D0RA06852G.
[58] D.H. Kang, G. Das, H.H. Yoon, I.T. Kim, A composite anion conducting membrane based on quaternized cellulose and poly(phenylene oxide) for alkaline fuel cell applications, Polymers 12 (2020) 2676, https://doi.org/10.3390/POLYM12112676.
[59] S. Hong, F. Al Marzooqi, J.K. El-Demellawi, N. Al Marzooqi, H.A. Arafat, H. N. Alshareef, Ion-selective separation using MXene-based membranes: a review, ACS Mater. Lett. 5 (2023) 341–356, https://doi.org/10.1021/ACSMATERIALSLETT.2C00914/ASSET/IMAGES/LARGE/TZ2C00914_0006.JPEG.
[60] L. Gao, C. Li, W. Huang, S. Mei, H. Lin, Q. Ou, Y. Zhang, J. Guo, F. Zhang, S. Xu, H. Zhang, MXene/polymer membranes: synthesis, properties, and emerging applications, Chem. Mater. 32 (2020) 1703–1747, https://doi.org/10.1021/ACS.CHEMMATER.9B04408/ASSET/IMAGES/MEDIUM/CM9B04408_0028.GIF.
[61] Z.E. AlHadithy, A.A. AbdulRazak, A.M.H.A. Al-Ghaban, Q.F. Alsalhy, H. Meskher, R.A. Al-Juboori, K.K. Katibi, D.U. Lawal, Advancements in water treatment with MXene-enhanced membranes: a review of current progress and future directions, Water Air Soil Pollut. (2024), https://doi.org/10.1007/S11270-024-07628-X, 235:12 235 (2024) 1–31.
[62] A. Çelik, Y. Aksoy, Ö. Hanay, M. Yegin, Y. Köse, K. Demirelli, H. Hasar, Fabrication and characterization of Ti3C2TX MXene-based bipolar membrane, J. Appl. Electrochem. (2024) 1–14, https://doi.org/10.1007/S10800-024-02231-8/METRICS.
[63] J. Li, X. Li, B. Van der Bruggen, An MXene-based membrane for molecular separation, Environ. Sci. Nano 7 (2020) 1289–1304, https://doi.org/10.1039/C9EN01478K.
[64] Y. Zheng, U. Ash, R.P. Pandey, A.G. Ozioko, J. Ponce-González, M. Handl, T. Weissbach, J.R. Varcoe, S. Holdcroft, M.W. Liberatore, R. Hiesgen, D.R. Dekel, Water uptake study of anion exchange membranes, Macromolecules 51 (2018) 3264–3278, https://doi.org/10.1021/ACS.MACROMOL.8B00034/SUPPL_FILE/MA8B00034_SI_001.PDF.
[65] S. Lakshmanan, V. Jurečič, V. Bobnar, V. Kokol, Dielectric and thermal conductive properties of differently structured Ti3C2Tx MXene-integrated nanofibrillated cellulose films, Cellulose 31 (2024) 8149–8168, https://doi.org/10.1007/S10570-024-06105-2/FIGURES/8.
[66] D. Parajuli, MXenes-polymer nanocomposites for biomedical applications: fundamentals and future perspectives, Front. Chem. 12 (2024) 1400375, https://doi.org/10.3389/FCHEM.2024.1400375.
[67] M. Dong, E. Bilotti, H. Zhang, D.G. Papageorgiou, Multifunctional Ti3C2Tx MXene-reinforced thermoplastic starch nanocomposites for sustainable packaging solutions, Int. J. Biol. Macromol. 265 (2024) 130520, https://doi.org/10.1016/J.IJBIOMAC.2024.130520.
[68] Q. Gao, M. Feng, E. Li, C. Liu, C. Shen, X. Liu, Mechanical, thermal, and rheological properties of Ti3C2Tx MXene/thermoplastic polyurethane nanocomposites, Macromol. Mater. Eng. 305 (2020) 2000343, https://doi.org/10.1002/MAME.202000343.
[69] H. Riazi, S.K. Nemani, M.C. Grady, B. Anasori, M. Soroush, Ti3C2 MXene–polymer nanocomposites and their applications, J. Mater. Chem. A Mater. 9 (2021) 8051–8098, https://doi.org/10.1039/D0TA08023C.
[70] T.K. Lee, J.H. Park, K.S. Im, S.K. Chitale, S.Y. Nam, Enhanced durability of carbazole-based anion exchange membranes via crosslinking and pore filling: fabrication and evaluation of anion exchange membrane water electrolysis, Int. J. Hydrogen Energy 176 (2025) 151441, https://doi.org/10.1016/J.IJHYDENE.2025.151441.
[71] Q. Xue, K. Zhang, The preparation of high-performance and stable MXene nanofiltration membranes with MXene embedded in the organic phase, Membranes 12 (2021) 2, https://doi.org/10.3390/MEMBRANES12010002.

[72] M. Nur-E-Alam, S.A. Deowan, E. Hossain, K.S. Hossain, M.Y. Miah, M. Nurnabi, Fabrication of polysulfone-based microfiltration membranes and their performance analysis, Water Air Soil Pollut. 235 (2024) 1–17, https://doi.org/10.1007/S11270-023-06872-X/METRICS.
[73] K.J. Peng, J.Y. Lai, Y.L. Liu, Preparation of poly (styrenesulfonic acid) grafted Nafion with a Nafion-initiated atom transfer radical polymerization for proton exchange membranes, RSC Adv. 7 (2017) 37255–37260, https://doi.org/10.1039/C7RA06984G.
[74] C. Long, C. Lu, Y. Li, Z. Wang, H. Zhu, N-spirocyclic ammonium-functionalized graphene oxide-based anion exchange membrane for fuel cells, Int. J. Hydrogen Energy 45 (2020) 19778–19790, https://doi.org/10.1016/J.IJHYDENE.2020.05.085.
[75] X. Mao, Z. Li, G. He, Z. Li, J. Zhao, Y. Zhang, Z. Jiang, Enhancing hydroxide conductivity of anion exchange membrane via incorporating densely imidazolium functionalized graphene oxide, Solid State Ion. 333 (2019) 83–92, https://doi.org/10.1016/J.SSI.2019.01.023.
[76] Q. Yang, C.X. Lin, F.H. Liu, L. Li, Q.G. Zhang, A.M. Zhu, Q.L. Liu, Poly (2,6-dimethyl-1,4-phenylene oxide)/ionic liquid functionalized graphene oxide anion exchange membranes for fuel cells, J. Membr. Sci. 552 (2018) 367–376, https://doi.org/10.1016/J.MEMSCI.2018.02.036.
[77] I. Arunkumar, A.R. Kim, S.H. Lee, D.J. Yoo, Enhanced fumion nanocomposite membranes embedded with graphene oxide as a promising anion exchange membrane for fuel cell application, Int. J. Hydrogen Energy 52 (2024) 139–153, https://doi.org/10.1016/J.IJHYDENE.2022.10.184.
[78] V. Vijayakumar, T.Y. Son, H.J. Kim, S.Y. Nam, A facile approach to fabricate poly (2,6-dimethyl-1,4-phenylene oxide) based anion exchange membranes with extended alkaline stability and ion conductivity for fuel cell applications, J. Membr. Sci. 591 (2019) 117314, https://doi.org/10.1016/J.MEMSCI.2019.117314.
[79] X. Yan, X. Yang, X. Su, L. Gao, J. Zhao, L. Hu, M. Di, T. Li, X. Ruan, G. He, Twisted ether-free polymer based alkaline membrane for high-performance water electrolysis, J. Power Sources 480 (2020) 228805, https://doi.org/10.1016/J.JPOWSOUR.2020.228805.
[80] M.J. Jang, J. Yang, J. Lee, Y.S. Park, J. Jeong, S.M. Park, J.Y. Jeong, Y. Yin, M. H. Seo, S.M. Choi, K.H. Lee, Superior performance and stability of anion exchange membrane water electrolysis: pH-controlled copper cobalt oxide nanoparticles for the oxygen evolution reaction, J. Mater. Chem. A Mater. 8 (2020) 4290–4299, https://doi.org/10.1039/C9TA13137J.
[81] B.C. Wyatt, M.G. Boebinger, Z.D. Hood, S. Adhikari, P.P. Michałowski, S. K. Nemani, M.G. Muraleedharan, A. Bedford, W.J. Highland, P.R.C. Kent, R. R. Unocic, B. Anasori, Alkali cation stabilization of defects in 2D MXenes at ambient and elevated temperatures, Nat. Commun. 15 (2024) 1–12, https://doi.org/10.1038/s41467-024-50713-2.
[82] S. Huang, V.N. Mochalin, MXene thermal and chemical stability and degradation mechanism, in: Transition Metal Carbides and Nitrides (MXenes) Handbook: Synthesis, Processing, Properties and Applications, 2024, pp. 137–162, https://doi.org/10.1002/9781119869528.CH7.
[83] L. Zhang, Y. Jiang, L. Zhou, Z. Jiang, L. Li, W. Che, Y. Yu, Mechanical, thermal stability, and flame retardancy performance of transparent wood composite improved with delaminated Ti3C2Tx (MXene) nanosheets, J. Mater. Sci. 57 (2022) 3348–3359, https://doi.org/10.1007/S10853-021-06776-3/METRICS.
[84] Z. Yu, W.C. Tsen, T. Qu, F. Cheng, F. Hu, H. Liu, S. Wen, C. Gong, Highly ion-conductive anion exchange membranes with superior mechanical properties based on polymeric ionic liquid filled functionalized bacterial cellulose for alkaline fuel cells, J. Mater. Res. Technol. 23 (2023) 6187–6199, https://doi.org/10.1016/J.JMRT.2023.02.197.
[85] H. Tang, D. Aili, R.A. Tufa, M.R. Kraglund, Q. Wu, C. Pan, L.N. Cleemann, Q. Li, Anion conductivity of cation exchange membranes in aqueous supporting electrolytes, Solid State Ion. 383 (2022) 115984, https://doi.org/10.1016/J.SSI.2022.115984.
[86] Y. Lei, J. Zhao, J. Gao, J. Wu, N. Li, X. Chi, Y. Wang, Y. Gu, Z. Wang, Robust branched poly (p-terphenyl isatin) anion exchange membranes with enhanced microphase separation structure for fuel cells, J. Membr. Sci. 713 (2025) 123368, https://doi.org/10.1016/J.MEMSCI.2024.123368.
[87] Z. Li, L. Gao, X. Wu, X. Jiang, X. Li, W. Xiao, W. Chen, W. Zheng, X. Ruan, X. Yan, G. He, Development of boosted microphase separation exploiting highly rigid poly(phenyl-alkane)s anion exchange membranes for excellent performance fuel cells, J. Power Sources 628 (2025) 235911, https://doi.org/10.1016/J.JPOWSOUR.2024.235911.
[88] Y. Zhang, J. Wu, S. Wang, J. Yu, Y. Gu, Y. Wang, J. Gao, C. Sun, Z. Li, Y. Lei, N. Li, J. Zhao, Z. Wang, Poly(p-terphenyl-piperidine-bromoacetophenone) anion exchange membranes with pendant N-spirocyclic cations: cations synergistic build efficient ion transport networks, J. Membr. Sci. 709 (2024) 123134, https://doi.org/10.1016/J.MEMSCI.2024.123134.
[89] J. Choi, K. Min, Y.H. Mo, S.B. Han, T.H. Kim, Understanding the effect of triazole on crosslinked PPO–SEBS-based anion exchange membranes for water electrolysis, Polymers (Basel) 15 (2023) 1736, https://doi.org/10.3390/POLYM15071736/S1.
[90] Z. Feng, G. Gupta, M. Mamlouk, Robust poly(p-phenylene oxide) anion exchange membranes reinforced with pore-filling technique for water electrolysis, J. Appl. Polym. Sci. 141 (2024) e55340, https://doi.org/10.1002/APP.55340.
[91] S.J. An, J.E. Kim, S. Yu, K.J. Kim, M.J. Kim, J.H. Kim, J.H. Lee, W.S. Chi, Ionic triptycene additive-blended poly(2,6-dimethyl-1,4-phenylene oxide)-based anion exchange membranes for water electrolyzers, ACS Appl. Energy Mater. 6 (2023) 8929–8940, https://doi.org/10.1021/ACSAEM.3C01538.
[92] X. Wang, Z. Fang, M. Zhang, S. Xie, D. Xie, P. Liu, S. Wang, F. Cheng, T. Xu, Macromolecular crosslinked poly(aryl piperidinium)-based anion exchange membranes with enhanced ion conduction for water electrolysis, J. Membr. Sci. 700 (2024) 122717, https://doi.org/10.1016/J.MEMSCI.2024.122717.
[93] Z. Feng, P.O. Esteban, G. Gupta, D.A. Fulton, M. Mamlouk, Highly conductive partially cross-linked poly(2,6-dimethyl-1,4-phenylene oxide) as anion exchange membrane and ionomer for water electrolysis, Int. J. Hydrogen Energy 46 (2021) 37137–37151, https://doi.org/10.1016/J.IJHYDENE.2021.09.014.
[94] Y. Lee, W. Lee, T.H. Kim, Enhancing the durability of anion exchange membrane water electrolysis cells via interfacial membrane–ionomer crosslinking, Bull. Korean Chem. Soc. 45 (2024) 620–630, https://doi.org/10.1002/BKCS.12881.
[95] Z. Jiang, G. Yi, X. Yao, Y. Ma, X. Su, Q. Liu, Q. Zhang, Durable and highly-efficient anion exchange membrane water electrolysis using poly(biphenyl alkylene) membrane, Chem. Eng. J. 467 (2023), https://doi.org/10.1016/j.cej.2023.143442.
[96] X. Lu, Y. Zhang, X. Ma, C. Yuan, Y. Chen, J. Guo, D. Gao, Y. Tu, Q. Liu, J. Wang, Z. Wei, Hydrogen bond network assisted ultrafast ion transport of anion exchange membrane grafting with covalent organic frameworks for hydrogen conversion, Angew. Chem. Int. Ed. 64 (2025) e202503372, https://doi.org/10.1002/ANIE.202503372.
[97] J. Ran, L. Wu, B. Wei, Y. Chen, T. Xu, Simultaneous enhancements of conductivity and stability for anion exchange membranes (AEMs) through precise structure design, Sci. Reports 4 (2014) 1–5, https://doi.org/10.1038/srep06486.
[98] S. Zheng, S. Zhao, Y. Liao, Y. Li, Z. Zhang, B. Liu, S. Wu, H. Tan, J. Ma, T. Tian, H. Tang, Durable and high-performance perfluorinated anion exchange membrane for pure-water-fed electrolysis, Int. J. Hydrogen Energy 101 (2025) 692–701, https://doi.org/10.1016/J.IJHYDENE.2024.12.498.
[99] J. Sang, L. Yang, Z. Li, F. Wang, Z. Wang, H. Zhu, Comb-shaped SEBS-based anion exchange membranes with obvious microphase separation morphology, Electrochim. Acta 403 (2022) 139500, https://doi.org/10.1016/J.ELECTACTA.2021.139500.
[100] Mohammad Mahbub Kabir, Yeshi Choden, Sherub Phuntsho, Leonard Tijing, Ho Kyong Shon, Advances in poly(phenylene oxide) (PPO)-based membranes for desalination, energy, and gas separation, Desalination 618 (2026) 119482, https://doi.org/10.1016/j.desal.2025.119482.
[101] Mohammad Mahbub Kabir, Yeshi Choden, Sherub Phuntsho, Leonard Tijing, Ho Kyong Shon, Predictive machine learning optimization of anion exchange membrane water electrolysis systems, Desalination 614 (2025) 119198, https://doi.org/10.1016/j.desal.2025.119198.
[102] M.M. Kabir, S.K. Roy, F. Alam, S.Y. Nam, K.S. Im, L. Tijing, H.K. Shon, Machine learning-based prediction and optimization of green hydrogen production technologies from water industries for a circular economy, Desalination 567 (2023) 116992, https://doi.org/10.1016/j.desal.2023.116992.
[103] Choden, Yeshi and Kabir, Mohammad Mahbub and Tijing, Leonard and Shon, Ho Kyong, Phuntsho, Sherub, Quaternized poly (phenylene oxide) - 3-Aminopropyl triethoxysilane functionalized ZrO2 nanocomposite anion exchange membranes for alkaline water electrolysis, Available at SSRN: https://ssrn.com/abstract=5550471 or https://doi.org/10.2139/ssrn.5550471 Quaternized poly (phenylene oxide) - 3-Aminopropyl triethoxysilane functionalized ZrO2 nanocomposite anion exchange membranes for enhanced alkaline water electrolysis in green hydrogen production. Available at SSRN: https://ssrn.com/abstract=5550471 or https://doi.org/10.2139/ssrn.5550471.